MATHEMATICAL METHODS FOR VORTEX IDENTIFICATION WITH APPLICATION ON SHOCK WAVE VORTEX RING INTERACTION

by

YINLIN DONG

Presented to the Faculty of the Graduate School of

The University of Texas at Arlington in Partial Fulfillment

of the Requirements

for the Degree of

DOCTOR OF PHILOSOPHY

THE UNIVERSITY OF TEXAS AT ARLINGTON

August 2017

Acknowledgements

First of all I would like to thank my research advisor and committee chairman, Dr. Chaoqun Liu, for his consistent guidance, advice, support, encouragement, patience and understanding in both academics and life throughout my years in Arlington, Texas.

I would also like to thank the committee members, Dr. Guojun Liao, Dr. Hristo Kojouharov, Dr. Ren-Cang Li, and Dr. David Liu, for their time and support.

I would like to acknowledge the help and support from the administrative faculty and staff of the Department of Mathematics at University of Texas at Arlington, especially Dr. Jianzhong Su, Dr. David Jorgensen, and Ms. Lona Donnelly. I appreciate the financial support from the Department through the Graduate Teaching Assistantships. I am also thankful to my colleagues for making my study at UTA a great experience.

My deepest gratitude goes to the love and meaning of my life: my wife, Ke Ma, my sons, Charles and Allen, and my parents, Yongliang Dong and Wenying Zhu. Thank you all for your lifelong support and care for me during the journey.

May 25, 2017

Abstract

MATHEMATICAL METHODS FOR VORTEX IDENTIFICATION

WITH APPLICATION ON SHOCK WAVE VORTEX RING INTERACTION

Yinlin Dong, Ph.D.

The University of Texas at Arlington, 2017

Supervising Professor: Chaoqun Liu

Vortices are seen everywhere in nature, from smoke rings to tornadoes. Vortical structures play an essential role in the turbulence dynamics such as turbulence generation, kinetic energy production and dissipation, enhancement of transport of mass, heat and momentum and so on.

In this dissertation, we present several vortex identification methods and compare them by the visualization of the examples studied by direct numerical simulation for flows with different speeds. The comparisons show the Omega method is much close to give vortex a mathematical definition and better visualization for vortical structures.

We apply our method on the Micro Vortex Generator (MVG) data to reveal the significant role of the transport of vortices in the shock wave boundary layer interaction. A wedge-shaped MVG is placed on a flat plate over which a turbulent boundary layer at Mach number 2.5 is developed. We investigate the interaction between an oblique shock and high-speed vortex rings in the MVG controlled ramp flow by using a high order implicit large eddy simulation with the fifth order bandwidth optimized WENO scheme. By tracking several typical vortex rings before, when and after they pass through the shock front, the quantitative changes of flow properties are studied in detail. The vortex ring propagation is found to be responsible for the shock motion, and thus cause the pulsation of the separation bubble. The shock ring interaction will provide an insight for the study of flow control.

Table of Contents

List of Illustrations

Chapter 1

Introduction

Vortices are seen everywhere in nature, which range from smoke rings to clouds, from hurricane to tornadoes, from swirl in the washing pool to whirlpools in the sea. One of the great challenges in fluid dynamics is to gain a comprehensive understanding of turbulent flows. A well-established approach is the analysis of the vortical structures contained in the flow. As has been shown both experimentally and numerically, vortical structures play an essential role in the turbulence dynamics such as turbulence generation, kinetic energy production and dissipation, enhancement of transport of mass, heat and momentum and so on. It is therefore important to understand the generation, interaction and evolution mechanisms of vortical structures.

Researchers have realized that turbulence is not a purely stochastic process, but a process with coherent vortical structures which play a decisive role in fluid dynamics and energy transport. Accurate visualization of vortices from huge amount of data obtained by experiments and numerical simulations becomes a key issue to solve the turbulence which is a century-long scientific problem. Using visualization techniques one should be able to observe and track the formation, convection and evolution of vortices in fluid flow transition and turbulent boundary layer. Vorticity, vorticity line and vorticity tube have rigorous definitions and we do not have much room to discuss, but the definition of vortex is still an open question. Various methods of identification and visualization of vortices have been proposed so far.

The common intuitive measures of vortex identification are inadequate. As has been discussed in Jeong & Hussain (1995), first, vorticity which is one of the most natural candidates for the characterization of vortical motions does not distinguish between shear layers and the swirling motion of vortices. The geometrical structure of the iso-surfaces of

the vorticity magnitude varies with the chosen value. Second, the existence of a local pressure minimum is neither a sufficient nor a necessary condition for the presence of a vortex. Third, the use of spiraling streamlines or pathlines is also problematic because they are not Galilean invariant, i.e., independent of the transitional velocity of an observer. Currently the most widely used techniques are the vortex identification methods based on the rotation nature of vortex, such as Δ method, Q method, swirling strength, λ_2 method, and Ω method.

The famous Q method was given by Hunt, Wray, and Moin (1988), in which a vortex is defined as the region with positive second invariant Q of the velocity gradient tensor $\nabla \boldsymbol{u}$. Actually Q represents the balance between shear strain rate and vorticity magnitude because $Q = \frac{1}{2}(||B||^2 - ||A||^2)$, where A and B are the symmetric and anti-symmetric components of $\nabla \boldsymbol{u}$. Another well-known scheme is the λ_2 method, developed by Jeong and Hussain (1995). They formed the equation for the Hessain of pressure from the incompressible Navier-Stokes equation then neglect the terms due to vorticity transport, irrotational straining and viscous effects. They suggested the usage of the second eigenvalue of the symmetric tensor $A^2 + B^2$ to capture the pressure minimum in a plane normal to the vortex axis. There are some other vortex identification methods but these two methods are popular and widely applied for vortex visualization. On the other hand, as demonstrated by Pierce, Moin and Sayadi (2013), the Δ, Q and λ_2 methods can provide the same graphics when applied to DNS data of a transitional boundary layer if iso-surface thresholds are chosen appropriately.

All these traditional vortex identification methods have a common critical weakness, which is the requirement of selecting a proper threshold. The threshold could be changed case by case, time by time, and even region by region in the same case. Different thresholds will lead to different vortical structures and no one is able to tell which

threshold is appropriate and which vortical structure is correct. The key issue is that we are still lack of more universal definition for vortex. A rotation with 2000 circles per second is a vortex but a rotation with 2 circles per second is also a vortex. However, if we use Q method or λ_2 method, we will be told that the weak rotation with 2 circles is not a vortex. If we adjust the threshold to include the rotation with 2 circles per second, the whole vortical structure of the flow field would be seriously smeared. Actually we are really not able to obtain correct vortical structure since different thresholds give different vortical structures.

A new method, called Omega vortex identification method, has been developed by Liu et al. (2016) which gives a more accurate mathematical definition for vortex and is pretty robust without requirement for a proper threshold. Ω measures the stiffness of fluid, which is a ratio of vorticity squared over the sum of vorticity squared and deformation squared. According to the ratio, vortex is defined when vorticity overtakes deformation or $\Omega > 0.5$. The iso-surface of $\Omega = 0.52$ is utilized to represent the vortex surface and further the vortical structure of the flow field.

One of the applications of vortex identification methods is in the topic of shock wave turbulent boundary layer interaction, which has been studied for over 60 years because of the major importance on the performance and safety of high-speed flight vehicles. Supersonic flow is different from subsonic compressible flow in that the flow is dominated by shock waves, typically on the order of 10^{-5} cm, across which there is an abrupt, nearly discontinuous change in flow properties like velocity, pressure, density, temperature, and Mach number. These shocks interact with the boundary layer and increase its thickness, resulting in large energy and total pressure loss, degraded engine system performance, and potentially flow distortion and separation.

A shock wave-boundary layer interaction with separation is inherently unstable. Shock instability is a well-known cause of air-intake buzz, which leads to large fluctuations in the thrust output and if not handled properly by the pilot can result in the engine to unstart. The traditional methods to control shock boundary layer interaction, like wall suction and bleed, are on the decline because bleed systems are heavy and complex, decrease mass flow to the engine and introduce additional drag. Lately, vortex generators are frequently employed to improve the boundary layer health because of their low weights and mechanical simplicity. These passive devices introduce streamwise vortices which transfer high momentum fluid from the freestream to the boundary layer and remove low momentum fluid from the near-wall region.

MVG (Micro vortex generator) is a low-profile passive control device designed for the boundary layer control. It can reduce the flow separation in compact ducts to some extent and control the boundary layer separation due to the adverse pressure gradients. In contrast to the conventional vortex generators whose heights match boundary layer thickness, MVG has a smaller size (a height approximately 20-40% of the boundary layer thickness), longer streamwise distance for the vortices to remain in the boundary layer, and better efficiency of momentum exchange.

The interaction of a vortex with a shock wave is one of the fundamental problems in fluid dynamics. In a supersonic flow, when a vortex meets the shock, disturbance is generated, which propagates further downstream and results in the back-reactions such as increase or decrease of vorticity and deformation of the shock wave. Such shock vortex interaction is important in the practical analysis and design of supersonic airplanes, missiles, rocket engines, wind tunnels, etc. Compared with the classic studies, the shock wave vortex ring interaction of the MVG controlled ramp flow is different in the followings: 1) the interaction is a more complicated three dimensional case rather than

the two dimensional counterpart; 2) the interaction is viewed as an instantaneous phenomenon rather than in a time-averaged sense; 3) the interaction happens within or close to the separation region where large scale vortices exist.

The shock induced boundary layer separation often leads to a highly unsteady flow field, which is characterized by a wide range of frequencies. The characteristic frequency near the shock foot is three orders of magnitude lower than the typical frequency of the incoming boundary layer and produces amplified wall pressure fluctuations which can cause strong buffeting of the underlying structure. The shock ring interaction can help to explain the source of the low-frequency unsteadiness and the large-scale pulsations of the separation bubble.

The structure of this dissertation is as follows. We first review and discuss the current vortex identification methods in Chapter 2. In Chapter 3, we compare two popular vortex identification methods, Q-criterion and λ_2 method, with the Omega method by visualization of several examples studied by direct numerical simulation (DNS) and large eddy simulation (LES) for flows with different speeds. In Chapter 4, we apply the Omega vortex identification method on the MVG controlled supersonic ramp flow to reveal the significant role of the transport of vortices in the shock wave vortex ring interaction. The conclusions and discussion will be given in Chapter 5.

Chapter 2

Vortex Identification Methods

2.1 Analysis of $\nabla \boldsymbol{u}$

The most widely used vortex identification methods are based on the analysis of the velocity gradient tensor $\nabla \boldsymbol{u}$. Let $\boldsymbol{u}$ be a 3D velocity field from which vortices are to be extracted. For every grid point of this vector field, $\nabla \boldsymbol{u}$ is computed and decomposed into a symmetric rate-of-strain tensor $A = (\nabla \boldsymbol{u} + \nabla \boldsymbol{u}^T)/2$ and an anti-symmetric rate-of-rotation tensor $B = (\nabla \boldsymbol{u} - \nabla \boldsymbol{u}^T)/2$, i.e.,

$$A = \begin{bmatrix} \frac{\partial u}{\partial x} & \frac{1}{2}(\frac{\partial u}{\partial y} + \frac{\partial v}{\partial x}) & \frac{1}{2}(\frac{\partial u}{\partial z} + \frac{\partial w}{\partial x}) \\ \frac{1}{2}(\frac{\partial u}{\partial y} + \frac{\partial v}{\partial x}) & \frac{\partial v}{\partial y} & \frac{1}{2}(\frac{\partial v}{\partial z} + \frac{\partial w}{\partial y}) \\ \frac{1}{2}(\frac{\partial u}{\partial z} + \frac{\partial w}{\partial x}) & \frac{1}{2}(\frac{\partial v}{\partial z} + \frac{\partial w}{\partial y}) & \frac{\partial w}{\partial z} \end{bmatrix}, \; B = \begin{bmatrix} 0 & -\frac{1}{2}(\frac{\partial u}{\partial y} - \frac{\partial v}{\partial x}) & -\frac{1}{2}(\frac{\partial u}{\partial z} - \frac{\partial w}{\partial x}) \\ \frac{1}{2}(\frac{\partial u}{\partial y} - \frac{\partial v}{\partial x}) & 0 & -\frac{1}{2}(\frac{\partial v}{\partial z} - \frac{\partial w}{\partial y}) \\ \frac{1}{2}(\frac{\partial u}{\partial z} - \frac{\partial w}{\partial x}) & \frac{1}{2}(\frac{\partial v}{\partial z} - \frac{\partial w}{\partial y}) & 0 \end{bmatrix}.$$

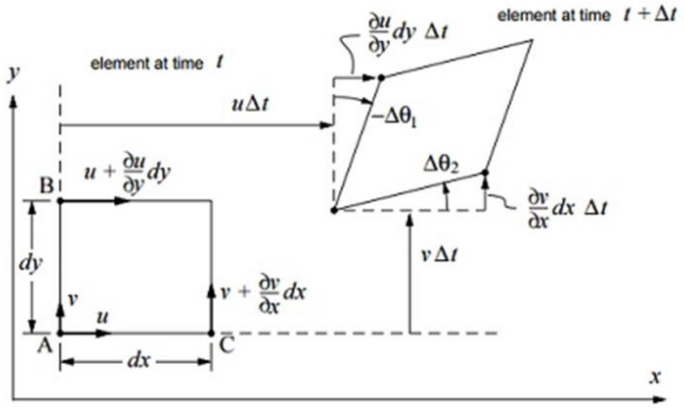

Figure 2-1 Fluid element from time t to $t + \Delta t$

Consider the 3D fluid element in the xy plane from time t to $t + \Delta t$ in Figure 2-1. Points A and B have an x-velocity which differs by $\frac{\partial u}{\partial y} dy$. Over the time interval Δt, the difference in the x-displacements is $\Delta x_B - \Delta x_A = \frac{\partial u}{\partial y} dy \Delta t$. The associated angle change

in side AB is $-\Delta\theta_1 = \frac{\Delta x_B - \Delta x_A}{dy} = \frac{\partial u}{\partial y}\Delta t$. The time rate of change of this angle is $\frac{d\theta_1}{dt} = \lim_{t\to 0}\frac{\Delta\theta_1}{\Delta t} = -\frac{\partial u}{\partial y}$. Similarly, the angle rate of change of side AC is $\frac{d\theta_2}{dt} = \frac{\partial v}{\partial x}$.

The angular velocity of the fluid element about the z-axis is defined as the average angular velocity of sides AB and BC

$$\omega_z = \frac{1}{2}\left(\frac{d\theta_1}{dt} + \frac{d\theta_2}{dt}\right) = \frac{1}{2}\left(\frac{\partial v}{\partial x} - \frac{\partial u}{\partial y}\right).$$

The same analysis in the xz and yz planes will give a 3D element's angular velocities ω_y and ω_x

$$\omega_y = \frac{1}{2}\left(\frac{\partial u}{\partial z} - \frac{\partial w}{\partial x}\right),\ \omega_x = \frac{1}{2}\left(\frac{\partial w}{\partial y} - \frac{\partial v}{\partial z}\right).$$

The vorticity vector is defined as twice of the angular velocity, i.e.,

$$\text{vorticity} \equiv 2\boldsymbol{\omega} = 2\left(\omega_x, \omega_y, \omega_z\right) = \left(\frac{\partial w}{\partial y} - \frac{\partial v}{\partial z}, \frac{\partial u}{\partial z} - \frac{\partial w}{\partial x}, \frac{\partial v}{\partial x} - \frac{\partial u}{\partial y}\right).$$

The vorticity tensor thus can be written as $B = \begin{bmatrix} 0 & \omega_z & -\omega_y \\ -\omega_z & 0 & \omega_x \\ \omega_y & -\omega_x & 0 \end{bmatrix}$.

Using the same fluid element and side angles $\Delta\theta_1$,$\Delta\theta_2$, we can define the strain (deformation) of the element by $\Delta\theta_2 - \Delta\theta_1$. The strain rate in the xy plane is then

$$\frac{d(\text{strain})}{dt} \equiv \varepsilon_{xy} = \frac{d\Delta\theta_2}{dt} - \frac{d\Delta\theta_1}{dt} = \frac{\partial v}{\partial x} + \frac{\partial u}{\partial y}.$$

Similarly, the rates of strain in the xz and yz planes are

$$\varepsilon_{xz} = \frac{\partial u}{\partial z} + \frac{\partial w}{\partial x}, \varepsilon_{yz} = \frac{\partial w}{\partial y} + \frac{\partial v}{\partial z}.$$

The rate-of-strain tensor thus can be written as $A = \begin{bmatrix} \frac{\partial u}{\partial x} & \varepsilon_{xy} & \varepsilon_{xz} \\ \varepsilon_{xy} & \frac{\partial v}{\partial y} & \varepsilon_{yz} \\ \varepsilon_{xz} & \varepsilon_{yz} & \frac{\partial w}{\partial z} \end{bmatrix}$.

Hence, the tensor A represents deformation while tensor B represents vorticity.

The three invariants of $\nabla \boldsymbol{u}$ based on the analysis of eigenvalues of $\nabla \boldsymbol{u}$ are used to classify the local streamline pattern around any point in a flow in a reference frame moving with the velocity of that point. The eigenvalues λ of $\nabla \boldsymbol{u}$ satisfy the characteristic equation $\det[\lambda I - \nabla \boldsymbol{u}] = 0$, i.e.,

$$\begin{vmatrix} \lambda - \frac{\partial u}{\partial x} & -\frac{\partial u}{\partial y} & -\frac{\partial u}{\partial z} \\ -\frac{\partial v}{\partial x} & \lambda - \frac{\partial v}{\partial y} & -\frac{\partial v}{\partial z} \\ -\frac{\partial w}{\partial x} & -\frac{\partial w}{\partial y} & \lambda - \frac{\partial w}{\partial z} \end{vmatrix} = 0.$$

The characteristic equation can be written as $\lambda^3 - P\lambda^2 + Q\lambda - R = 0$, where P, Q and R are the three invariants of $\nabla \boldsymbol{u}$, and

$$P = \frac{\partial u}{\partial x} + \frac{\partial v}{\partial y} + \frac{\partial w}{\partial z} = \mathrm{tr}(\nabla \boldsymbol{u}) = \nabla \cdot \boldsymbol{u},$$

$$Q = \begin{vmatrix} \frac{\partial u}{\partial x} & \frac{\partial u}{\partial y} \\ \frac{\partial v}{\partial x} & \frac{\partial v}{\partial y} \end{vmatrix} + \begin{vmatrix} \frac{\partial u}{\partial x} & \frac{\partial u}{\partial z} \\ \frac{\partial w}{\partial x} & \frac{\partial w}{\partial z} \end{vmatrix} + \begin{vmatrix} \frac{\partial v}{\partial y} & \frac{\partial v}{\partial z} \\ \frac{\partial w}{\partial y} & \frac{\partial w}{\partial z} \end{vmatrix} = \frac{(\nabla \cdot \boldsymbol{u})^2 - \mathrm{tr}(\nabla \boldsymbol{u})^2}{2},$$

and $R = \det(\nabla \boldsymbol{u})$.

2.2 Δ Method

Using critical point theory Chong et al. (1990) defined a vortex core to be the connected region in which $\nabla \boldsymbol{u}$ has complex eigenvalues. The streamlines in the vicinity of a point $\boldsymbol{r}$ in a reference frame moving with the velocity at $\boldsymbol{r}$ are given by

$$\frac{\mathrm{d}(\delta \boldsymbol{r})}{\mathrm{d}t} = (\nabla \boldsymbol{u}) \delta \boldsymbol{r},$$

which has the solution

$$\delta \boldsymbol{r} = c_1 \exp(\lambda_1 t)\, \boldsymbol{e}_1 + c_2 \exp(\lambda_2 t)\, \boldsymbol{e}_2 + c_3 \exp(\lambda_3 t)\, \boldsymbol{e}_3,$$

where λ_i and $\boldsymbol{e}_i$ are the eigenvalues and eigenvectors of $\nabla \boldsymbol{u}$. Complex eigenvalues of $\nabla \boldsymbol{u}$ will result in spiraling streamlines.

If $\nabla \boldsymbol{u}$ has complex eigenvalues, then it can be transformed to the canonical form $\begin{pmatrix} a & -\omega & 0 \\ \omega & a & 0 \\ 0 & 0 & b \end{pmatrix}$, where $\lambda_{1,2} = a \pm i\omega$, and $\lambda_3 = b$. The sign of b determines whether the streamline trajectory is directed away or toward the plane of the focus. If b>0, the spiraling is away from the focus plane; if b<0, the spiraling is toward the focus plane.

For an impressive flow, $P = \nabla \cdot \boldsymbol{u} = 0$. The discriminant of the characteristic equation is given by $\Delta = (Q/3)^3 + (R/2)^2$. Complex eigenvalues of $\nabla \boldsymbol{u}$ thus vortices occur when the discriminant $\Delta > 0$.

2.3 Q Method

Hunt et al. (1988) identified vortices as flow regions with positive second invariant of $\nabla \boldsymbol{u}$, i.e., $Q > 0$. In addition, the pressure in the vortex region is required to be lower than the ambient value. For an incompressible flow, Q can be written as

$$Q = \frac{1}{2}(||B||^2 - ||A||^2),$$

where $||A||^2 = \mathrm{tr}(AA^T)$ and $||B||^2 = \mathrm{tr}(BB^T)$.

According to this method, a flow region appears as a vortex if the local rate-of-rotation is larger than the rate-of-strain, i.e., the antisymmetric part of $\nabla \boldsymbol{u}$ is prevailing over the symmetric part. It can be seen that the Q method is more restrictive than the Δ method.

2.4 Swirling Strength

Zhou et al. (1999) used the imaginary part of the complex eigenvalue of $\nabla \boldsymbol{u}$ to visualize vortices and to quantify the strength of the local swirling motion inside the vortex. When $\nabla \boldsymbol{u}$ has complex eigenvalues, they can be denoted by $\lambda_{cr} \pm i\lambda_{ir}$. The "swirling strength", given by λ_{ci}, is a measure of the local swirling rate inside the vortex.

The strength of stretching or compression is determined by the real eigenvalue λ_{cr}. As we can see, this method is based on the Δ method, however, it identifies not only the vortex region, but also the local strength and the local plane of swirling. It may be noted that although $\Delta = 0$ and $\lambda_{ci} = 0$ are equivalent, for the nonzero thresholds the results may be significantly different.

2.5 λ_2 Method

The λ_2 method was proposed by Jeong & Hussain (1995) and is popular due to its reliability in detecting vortices and the simplicity of the operations involved in the computation. By neglecting the unsteady irrotational straining and viscous effects, the symmetric part of the gradient of the incompressible Navier–Stokes equation can be expressed as

$$A^2 + B^2 = -\frac{1}{\rho}\nabla^2 p.$$

Hence $A^2 + B^2$ determines the existence of a local pressure minimum. This matrix is real and symmetric and thus has exactly three real eigenvalues. These eigenvalues are computed and sorted in the decreasing order: $\lambda_1 \geq \lambda_2 \geq \lambda_3$. A vortex is then defined as a connected region where two of the eigenvalues are negative, which is equivalent to the condition $\lambda_2 < 0$. The eigenvalues of $A^2 + B^2$ and Q are related by

$$Q = \frac{1}{2}(||B||^2 - ||A||^2) = -\frac{1}{2}\mathrm{tr}(A^2 + B^2) = -\frac{1}{2}(\lambda_1 + \lambda_2 + \lambda_3).$$

Note that the λ_2 method is built on the N-S equation and viscous effects are ignored, while the Δ and Q methods are directly derived from $\nabla \boldsymbol{u}$ for arbitrary flows without any assumptions. While the Q method measures the excess of rotation rate over the strain rate magnitude in all directions, the λ_2 method looks for this excess only on a specific plane.

For visualization, since for every grid point a corresponding λ_2 value can be computed, the λ_2 method transforms the original vector field into a scalar volume which can then be visualized by any volume visualization technique, most commonly iso-surfaces.

2.6 Hybrid of λ_2 and Vorticity Lines

2.6.1 Fake Vortex Breakdown Caused by Improper λ_2

There is no fixed threshold for Δ, Q and λ_2. Take λ_2 for example. The output of the λ_2 method is a scalar field which sees vortices as regions. Different values of λ_2 will give different iso-surfaces which identify different vortical structures. By selecting improper λ_2 values, we may obtain some non-physical vortical structures, i.e., fake vortex breakdown.

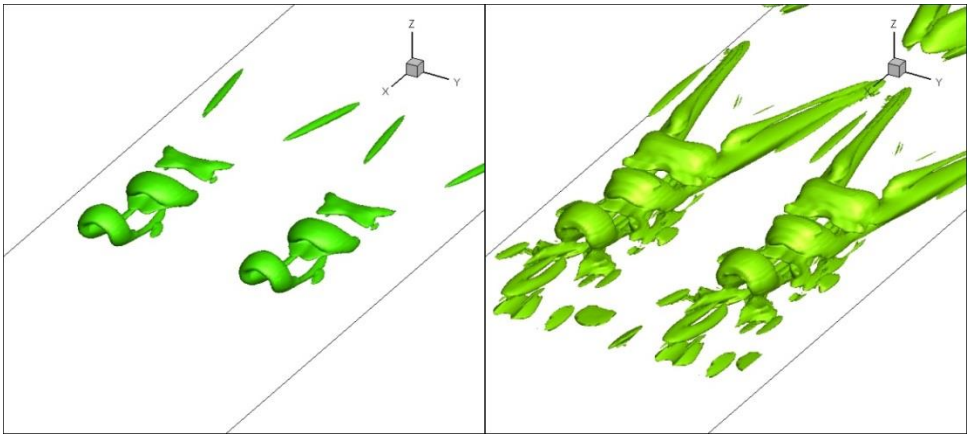

(a) (b)

Figure 2-2 Vortical structure in transition flows by iso-surface of λ_2

(a) $\lambda_2 = -0.02$ (b) $\lambda_2 = -0.001$

Figure 2-2 shows the vortical structure from our study of the late transition flows by DNS data. The vortical structure is illustrated by the iso-surface of $\lambda_2 = -0.02$ at the time t = 6.5T (T is the period of the T-S wave) in (a) and $\lambda_2 = -0.001$ at the same time in (b). From (a), the vortices seem to break down. However, if we choose a different λ_2

value, for the same data set, we can easily make another λ_2 iso-surface which links vortices altogether as shown in (b). In other words, the vortical structure is stable and never breaks down.

Nevertheless, λ_2 captures the pressure minimum in a plane across the vortex, which helps us to find a general location of the vortex core. To obtain more accurate vortical structures from turbulent flows, one needs to combine λ_2 with the track of vortex filaments.

2.6.2 Use of Vortex Filaments

A vortex filament can be viewed as a vortex tube of infinitesimal cross section. It is located at the geometric center of the vorticity distribution. Vorticity is defined as the curl of the velocity field and related to the rotation rate of the fluid element in fluid dynamics. The vorticity line is a curve which is everywhere tangent to the local vorticity vector ($\nabla \times \boldsymbol{u}$). From any point in the flow field, we can generate a vorticity line that passes through it. Vortex filaments are vorticity lines in the vortex tube, which is a bundle of vorticity lines without any vorticity leakage. The vortex filament is an attractive fluid dynamic concept which allows simple understanding of a large part of the entire flow.

Intuitively, a vortex is concentrated along a vortex filament in the flow and vortex filaments have advantages in presenting the turbulence structures. However, vortex filaments are generally chaotic in three dimensional flows and their topology is structurally unsteady. Using vortex filaments alone as a means of visualization would not be advantageous, because they have the disadvantage that no distinction is made between vortices and shear layers, and that regions with small vorticity cannot be distinguished from regions with large vorticity. The diffusion by viscosity, coupled with the interaction of vorticity distribution with strain field, makes the problem of identifying vortex filaments in real fluids quite complicated. In Figure 2-3, we generate the vortex filaments

in the same database of Figure 2-2 spatially. Although the vortex filaments show some of the flow pattern in the lower boundary layer, the vivid vortical structure is not even sketched by those vortex filaments.

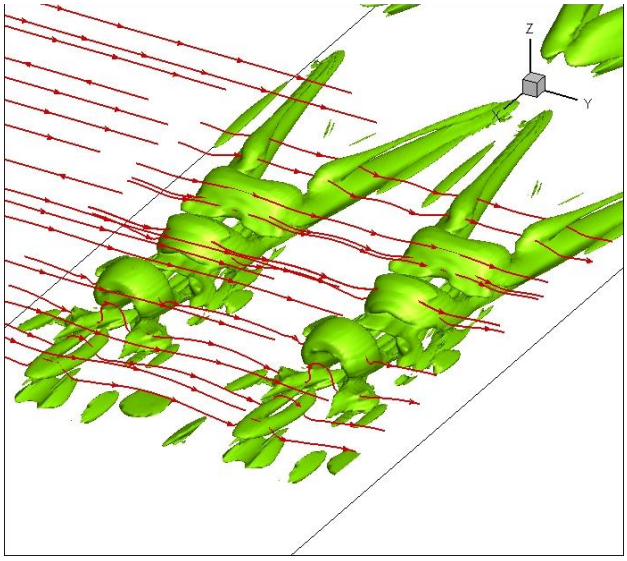

Figure 2-3 Vortical structure in transition flows by iso-surface of λ_2
and the surrounding vortex filaments

Therefore we cannot identify vortex structures clearly just by tracking vortex filaments. This makes us to seek a method combining the use of vortex filaments with the advantages of the λ_2 method.

2.6.3 Hybrid of λ_2 and Vortex Filaments

By adjusting different values, the λ_2 iso-surface could break down and sometimes could not represent the true vortical structure. Some vortex structure may exist but could not be visualized by the λ_2 method because the rate of rotation of the vortices must be strong enough to be detected and shown on the λ_2 iso-surface. On the other hand, if the value of λ_2 is selected as too close to 0, too many details may be given by the λ_2 iso-surface, which makes the vortex structure very complicated and difficult to find the origin.

This, however, is insufficient since researchers either want to see a certain vortex or do not want to see certain vortices being irrelevant for the special application or obscuring the region of interest. Our approach to alleviate these drawbacks is to combine the λ_2 method with the track of vortex filaments.

We first capture the vortex core by a proper λ_2 value, which means such a value will not cause fake vortex breakdown. Vortex filaments are vorticity lines inside the vortex core. Vorticity lines outside vortex cores are not called filaments and not our interest. We identify vortex filaments through the λ_2 method with low-pressure cores. We select points inside the λ_2 iso-surface and then track the vortex filaments to find the origin of these vortices. In this way, we can not only identify and visualize the vortical structure but also track the formation and evolution of the vortices.

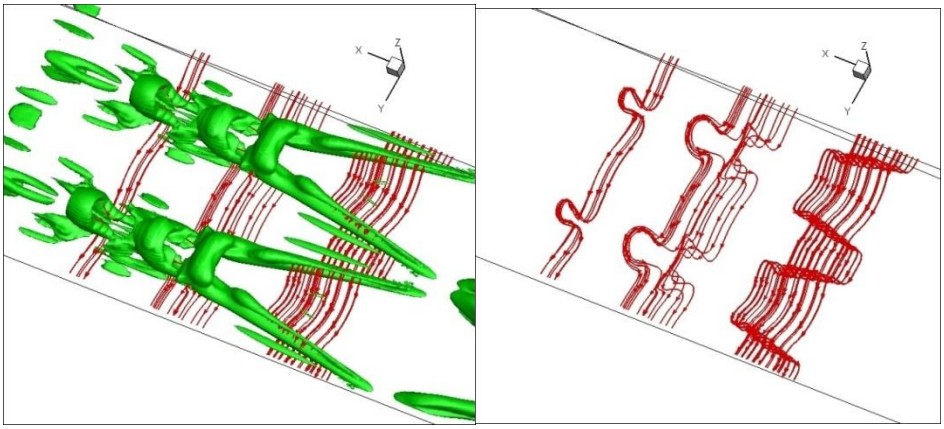

Figure 2-4 Vortical structure in transition flows by iso-surface of λ_2 and the track of vortex filaments

To illustrate, on the left of Figure 2-4, the Λ-vortices are depicted in terms of properly selected λ_2 iso-surfaces. Inside the λ_2 iso-surfaces, vortex filaments originated from different positions are also demonstrated and these filaments become much denser at the places where a λ_2 iso-surface is visualized. In the right figure, by dropping the λ_2

iso-surfaces, we can see more clearly that the vortex filaments aggregate at the center of the legs of the Λ-vortices as a result of the stretching effect. By tracking the vortex filaments, we find that the filaments originate from one side of the so-called Λ-vortices, penetrate the Λ-vortices and move up and down aligned with the λ_2 iso-surfaces, and end in the other side of the Λ-vortices. We conclude that the origin of the Λ-vortices comes from the sides of the spanwise direction and Λ-vortices are not the vortex tubes since vortex filaments cannot penetrate the vortex tubes in any cases.

2.7 Ω Method

2.7.1 Definition of Ω

Liu et al. (2016) proposed a further decomposition of the vorticity to vortical part and non-vortical part after reviewing Helmholtz velocity decomposition and some counterexamples like Blasius solution which has large vorticity but has no vortex. Ω measures the stiffness of fluid and is a ratio of trace of anti-symmetric tensor squared over the sum of traces for both symmetric and anti-symmetric tensors squared, i.e.,

$$\Omega = \frac{\mathrm{Trace}(B^T B)}{\mathrm{Trace}(A^T A) + \mathrm{Trace}(B^T B) + \varepsilon},$$

where A is the symmetric part of velocity gradient tensor $\nabla \boldsymbol{u}$, B is the anti-symmetric part, and $\boldsymbol{\varepsilon}$ is a small positive number to avoid division by zero.

By this definition, Ω is always between 0 and 1 since A and B are nonnegative. If rotation is quite dominant, then Ω is very close to 1, which is like a solid body. If fluid has strong shear without rotation, then Ω is near 0. Thus Ω is a measurement of fluid stiffness. A vortex is defined as a region where vorticity overtakes deformation, i.e., $\Omega > 0.5$. The larger the value of Ω, the faster the rotation at that region, and vice versa.

Different from Q and λ_2 methods which require a proper threshold to capture the vortices, the Ω method is quite universal and has no need to set up a threshold case by

case, region by region, or even time by time in the same case. The iso-surface of $\Omega = 0.52$ can always capture the vortices in all cases that we investigate. Also, both strong and weak vortices can be well captured simultaneously by the Ω method.

2.7.2 Tensor Analysis of Ω Iso-surface

We obtain the velocity gradient tensor from our DNS data at the point $x = 452$ at $t = 5.08T$, i.e.,

$$\nabla \boldsymbol{u} = \begin{bmatrix} 0.0046518 & -0.0457264 & 0.494155 \\ 0.0105014 & 0.000920 & -0.099773 \\ -0.003065 & 0.0053967 & -0.005662 \end{bmatrix}.$$

First we decompose $\nabla \boldsymbol{u}$ into the rate-of-strain tensor A and the vorticity tensor B.

$$A = \begin{bmatrix} 0.004652 & -0.017612 & 0.245545 \\ -0.17612 & 0.000920 & -0.047188 \\ 0.245545 & -0.047188 & -0.005662 \end{bmatrix}, \; B = \begin{bmatrix} 0 & 0.028114 & -0.497219 \\ -0.028114 & 0 & 0.052585 \\ 0.497219 & -0.052585 & 0 \end{bmatrix}.$$

Then we compute $\mathrm{tr}(AA^T) = 0.425713$ and $\mathrm{tr}(BB^T) = 0.501566$. By definition, Ω is found to be 0.5298, which means at this point vorticity overtakes deformation. The point should be contained in the iso-surface of vortex.

Hence, Ω is a function of the point position in the three dimensional flow field. Ω can identify the existence of vortices universally and make it possible to represent the appearance of vortices mathematically. This is an unprecedented effort to provide a quantitative way to study the flow properties involving the evolution of vortices, such as in the time signal and frequency analysis, which will be discussed more in Chapter 4.

Chapter 3

Comparisons of Methods

We will compare the Ω method with the Q and λ_2 methods for the same data set at the same time step. We first implement the three methods on the case of the late boundary layer transition obtained from our DNS data. An MVG case is also used to evaluate the various identification methods.

3.1 Late Boundary Layer Transition

3.1.1 Case Setup

The governing system is the three dimensional compressible Navier-Stokes equations in generalized curvilinear coordinates in a conservative form, i.e.,

$$\frac{1}{J}\frac{\partial Q}{\partial t}+\frac{\partial (E-E_v)}{\partial \xi}+\frac{\partial (F-F_v)}{\partial \eta}+\frac{\partial (G-G_v)}{\partial \zeta}=0.$$

J is the Jacobian of the coordinate transformation between the curvilinear (ξ,η,ζ) and Cartesian (x,y,z). The conserved vector Q, the inviscid flux vector (E,F,G), and the viscous flux vector are defined as

$$Q=\begin{pmatrix}\rho\\ \rho u\\ \rho v\\ \rho w\\ e\end{pmatrix}, E=\frac{1}{J}\begin{pmatrix}\rho U\\ \rho uU+p\xi_x\\ \rho vU+p\xi_y\\ \rho wU+p\xi_z\\ U(e+p)\end{pmatrix}, F=\frac{1}{J}\begin{pmatrix}\rho V\\ \rho uV+p\eta_x\\ \rho vV+p\eta_y\\ \rho wV+p\eta_z\\ V(e+p)\end{pmatrix}, G=\frac{1}{J}\begin{pmatrix}\rho W\\ \rho uW+p\zeta_x\\ \rho vW+p\zeta_y\\ \rho wW+p\zeta_z\\ W(e+p)\end{pmatrix},$$

$$E_v=\frac{1}{J}\begin{pmatrix}0\\ \tau_{xx}\xi_x+\tau_{yx}\xi_y+\tau_{zx}\xi_z\\ \tau_{xy}\xi_x+\tau_{yy}\xi_y+\tau_{zy}\xi_z\\ \tau_{xz}\xi_x+\tau_{yz}\xi_y+\tau_{zz}\xi_z\\ q_x\xi_x+q_y\xi_y+q_z\xi_z\end{pmatrix}, F_v=\frac{1}{J}\begin{pmatrix}0\\ \tau_{xx}\eta_x+\tau_{yx}\eta_y+\tau_{zx}\eta_z\\ \tau_{xy}\eta_x+\tau_{yy}\eta_y+\tau_{zy}\eta_z\\ \tau_{xz}\eta_x+\tau_{yz}\eta_y+\tau_{zz}\eta_z\\ q_x\eta_x+q_y\eta_y+q_z\eta_z\end{pmatrix},$$

$$G_v=\frac{1}{J}\begin{pmatrix}0\\ \tau_{xx}\zeta_x+\tau_{yx}\zeta_y+\tau_{zx}\zeta_z\\ \tau_{xy}\zeta_x+\tau_{yy}\zeta_y+\tau_{zy}\zeta_z\\ \tau_{xz}\zeta_x+\tau_{yz}\zeta_y+\tau_{zz}\zeta_z\\ q_x\zeta_x+q_y\zeta_y+q_z\zeta_z\end{pmatrix},$$

where ρ is the flow density, (u, v, w) is the velocity field, e is the total energy, p is the flow pressure, $\xi_x, \xi_y, \xi_z, \eta_x, \eta_y, \eta_z, \zeta_x, \zeta_y, \zeta_z$ are coordinate transformation metrics, U, V, W are the contravariant velocity components defined as $U = u\xi_x + v\xi_y + w\xi_z, V = u\eta_x + v\eta_y + w\eta_z, W = u\zeta_x + v\zeta_y + w\zeta_z$, $\tau_{xx}, \tau_{yy}, \tau_{zz}, \tau_{xy}, \tau_{xz}, \tau_{yz}$ are components of viscous stress, and q_x, q_y, q_z are components of heat flux.

In the dimensionless form of the N-S equations, the reference values for length, density, velocity, temperature and pressure are $\delta_{in}, \rho_\infty, U_\infty, T_\infty$ and $\rho_\infty U_\infty^2$. The Mach number and Reynolds number are expressed as

$$M_\infty = \frac{U}{\sqrt{\gamma R T_\infty}}, Re = \frac{\rho_\infty U_\infty \delta_{in}}{\mu_\infty},$$

where R is the ideal gas constant, γ is the ratio of specific heats, δ_{in} is the inflow displacement thickness, and μ_∞ is the viscosity.

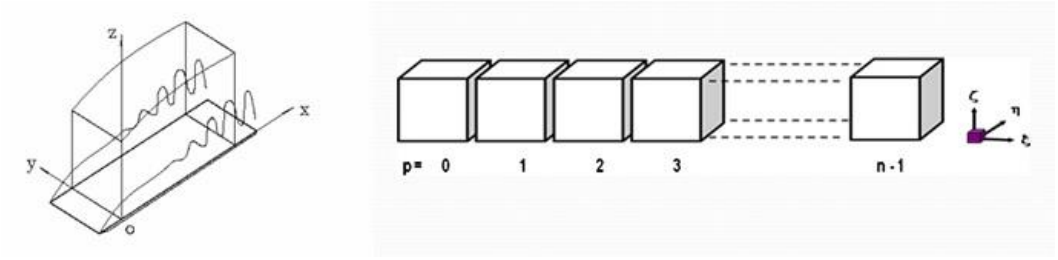

Figure 3-1 The computational domain of the DNS case

The computational domain is shown in Figure 3-1. The grid level in the streamwise (x), spanwise (y) and wall normal direction (z) is 1920×128×241. The grid is stretched in the normal direction and uniform in the streamwise and spanwise directions. The parallel computation is accomplished through the Message Passing Interface (MPI) along with a domain decomposition in the streamwise direction. The computation domain is partitioned into n equal sub-domains in the streamwise direction. Here, n is the number of processors used in the parallel computation.

3.1.2 Numerical Methods

A six order compact scheme is used for the spatial discretization in the streamwise and wall normal directions, i.e.,

$$\frac{1}{3}f'_{j-1} + f'_j + \frac{1}{3}f'_{j+1} = \frac{1}{h}\left(-\frac{1}{36}f_{j-2} - \frac{7}{9}f_{j-1} + \frac{7}{9}f_{j+1} + \frac{1}{36}f_{j+2}\right),$$

for the interior points $j = 3, \cdots, N-2$. The fourth order compact scheme is used at points $j = 2, N-1$, and the third order one-sided compact scheme is used on the boundary.

In the spanwise direction where periodic conditions are applied, the pseudo-spectral method is used to compute the derivatives. In order to eliminate the spurious numerical oscillations caused by central difference schemes, a high-order spatial scheme is used instead of artificial dissipation. An implicit sixth-order compact scheme for space filtering is applied to the primitive variables u, v, w, ρ, p after a specified number of time steps.

The adiabatic, zero-gradient pressure and no-slip conditions are enforced on the wall boundary. The inlet boundary condition is an enforced disturbance including 2D and 3D T-S waves. On the far field and outflow boundaries, the non-reflecting boundary conditions are applied.

The governing equations are solved explicitly in time by a third order total variation diminishing Runge-Kutta scheme:

$$Q^{(0)} = Q^n,$$

$$Q^{(1)} = \Delta t\, R^{(0)},$$

$$Q^{(2)} = \frac{3}{4}Q^{(0)} + \frac{1}{4}Q^{(1)} + \frac{1}{4}\Delta t\, R^{(1)},$$

$$Q^{n+1} = \frac{1}{3}Q^{(0)} + \frac{2}{3}Q^{(2)} + \frac{2}{3}\Delta t\, R^{(2)}.$$

The condition $CFL \ll 1$ is required to ensure the stability.

3.1.3 Code Validation

The skin-friction coefficients calculated from the time and spanwise averaged profile on a coarse and fine grid is displayed in Figure 3-2. The spatial evolution of skin-friction coefficients of laminar flow is also plotted out for comparison. It is observed from these figures that the sharp growth of the skin-friction coefficient occurs after $x \approx 450\delta_{in}$, which is defined as the "onset point". The skin-friction coefficient after transition is in good agreement with the flat-plate theory of turbulent boundary layer by Cousteix (1989). Figure 3-2 also shows a grid convergence in skin-friction coefficients is obtained.

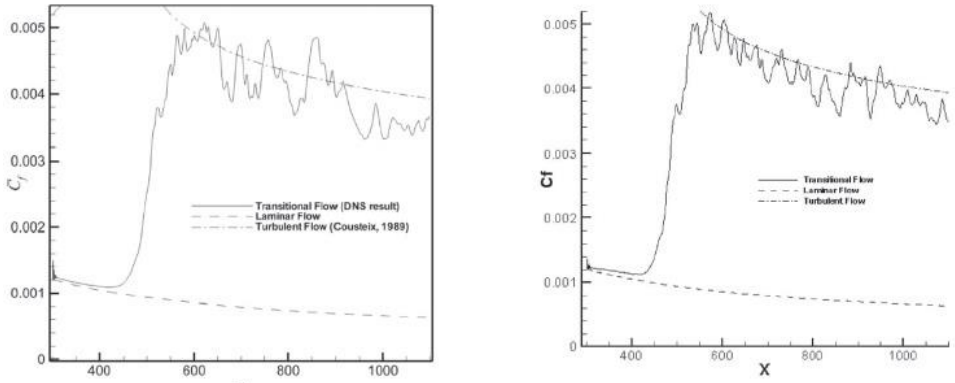

(a) (b)

Figure 3-2 Streamwise evolutions of the time and spanwise averaged skin-friction coefficients (a) coarse grids (960×64×121) (b) fine grids (1920×128×241)

Time and spanwise averaged streamwise velocity profiles for various streamwise locations in two different grid levels are shown in Figure 3-3.The inflow velocity profiles at $x = 300.79\delta_{in}$ is a typical laminar flow velocity profile. At $x = 632.33\delta_{in}$, the mean velocity profile approaches a turbulent flow velocity profile (Log Law). This comparison shows that the velocity profile from the DNS results in a turbulent flow velocity profile and the grid convergence has been realized.

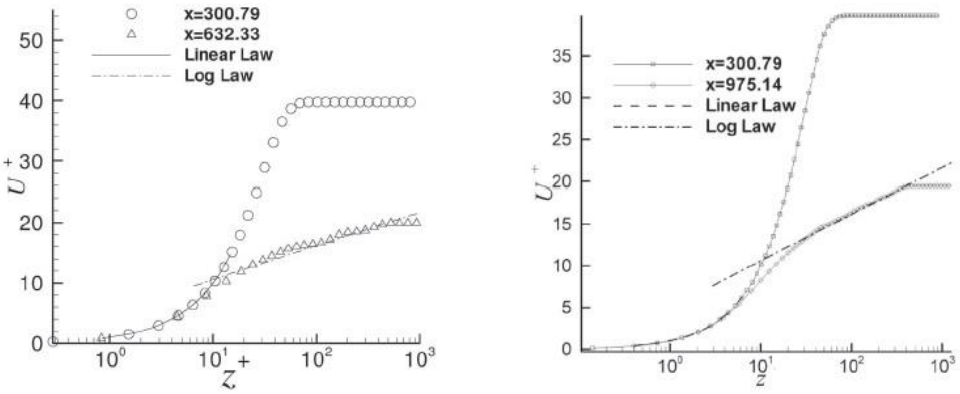

(a) (b)

Figure 3-3 Log-linear plots of the time and spanwise averaged velocity profile in wall unit (a) coarse grids (960×64×121) (b) fine grids (1920×128×241)

Figure 3-4 compares our DNS results with the data set provided by Rist (2012), showing the same vortex structure visualized by the hybrid of λ_2 and vortex filaments. Figure 3-5 gives a qualitative comparison of streamwise velocity disturbance between our DNS results and those provided by Borodulin et al. (2002). A similarity in the shear layer structure can be found in the two DNS computations.

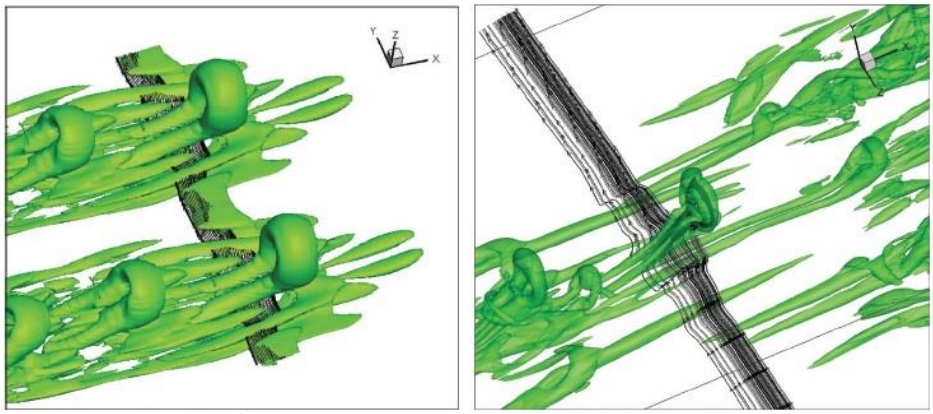

(a) (b)

Figure 3-4 Comparison of our DNS results with Rist's DNS data using λ_2 and vortex filaments (a) Our DNS (b) Rist's DNS

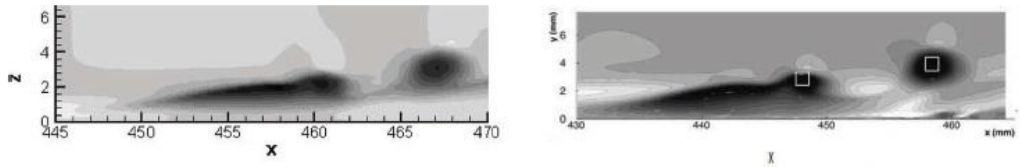

(a) (b)

Figure 3-5 Qualitative comparison of contours of streamwise velocity disturbance in the xz-plane (a) Our DNS (b) Borodulin et al.

All the above verifications and validations show that our code is correct and our DNS results are reliable.

3.1.4 Comparison at an Early Time Step

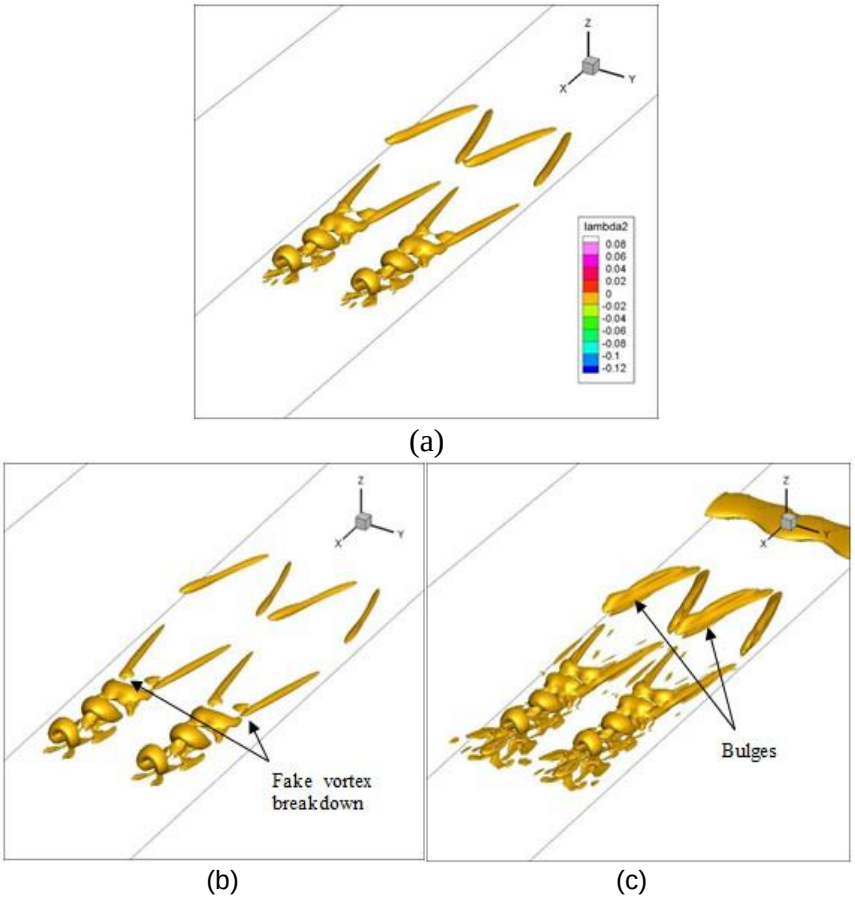

(a)

(b) (c)

Figure 3-6 Iso-surfaces of (a) $\lambda_2 = -0.005$ (b) $\lambda_2 = -0.01$ (c) $\lambda_2 = -0.001$

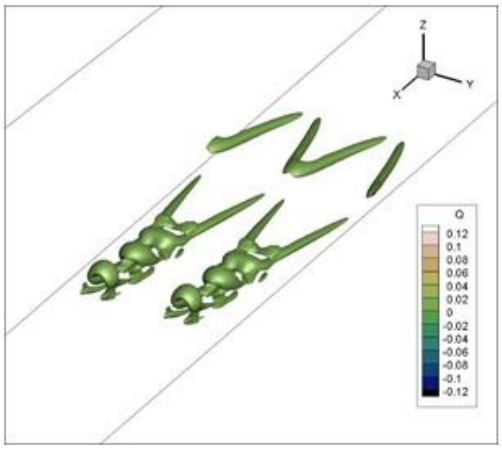

(a)

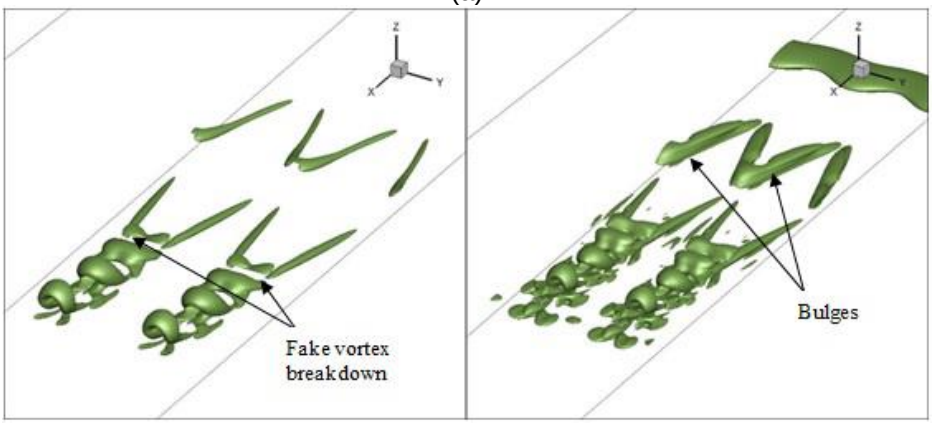

(b) (c)

Figure 3-7 Iso-surfaces of (a) $Q = 0.005$ (b) $Q = 0.01$ (c) $Q = 0.001$

First we look at the λ_2, Q and Ω methods when Λ vortices and hairpin vortices start to form in the late boundary layer transition. Figure 3-6 shows the vortex structures given by the iso-surfaces of $\lambda_2 = -0.005$, $\lambda_2 = -0.01$ and $\lambda_2 = -0.001$ at an early time step t = 666. Figure 3-7 shows the iso-surfaces of $Q = 0.005$, $Q = 0.01$ and $Q = 0.001$ at the same time step.

We see that the vortex structures are almost the same based on the Q method and λ_2 method. This is because these two quantities are related by $Q = -\frac{1}{2}(\lambda_1 + \lambda_2 + \lambda_3)$. If Q is positive, the middle eigenvalue λ_2 is most likely negative, and vice versa.

It is difficult or sometimes time-consuming to choose the appropriate thresholds for both λ_2 and Q methods. What we want is (1) the vortex structures should be identified correctly; (2) the main structures should be clear; (3) the visualization should not lose so many secondary vortices. Based on such criteria, the parts (b) in Figures 3-6 and 3-7 give "fake vortex breakdown". However, if we adjust a different threshold as in parts (a), we can clearly see that the vortex structures represent actually the legs of the Λ-vortices. The structures are very stable and never break down.

The parts (c) in Figures 3-6 and 3-7 seem to capture the vortex structures well, but the main structures are not as clear as those shown in parts (a). Furthermore, there are some "bulges" above the Λ-vortex which might be thought as part of the Λ-vortex since another vortex layer seems to be on the top of the Λ-vortex in parts (c), but these structures are not identified in parts (a).

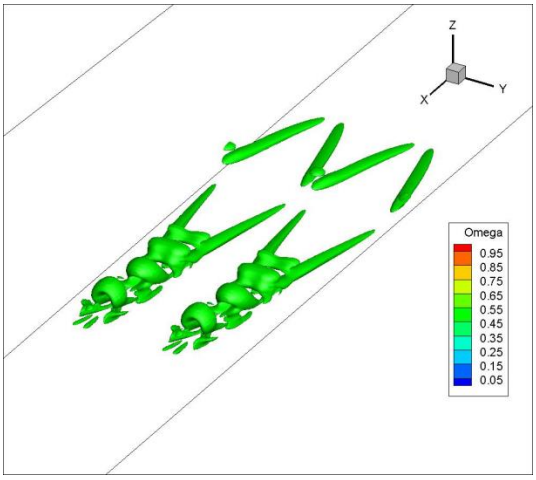

Figure 3-8 Iso-surface of $\Omega = 0.52$

Hence, the parts (a) give the most accurate visualization of the vortex structures in the late boundary layer transition. The larger magnitude of λ_2 and Q may cause fake vortex breakdown, while the smaller magnitude of λ_2 and Q may smear the vortex structures, making the vortices indistinguishable from each other. Here the questions

arise. How do we know which thresholds of λ_2 and Q will capture the accurate vortex structures? What are the physical meanings of the different λ_2 and Q values?

Applying the Omega method, Figure 3-8 shows the iso-surface of $\Omega = 0.52$ at the same time step t = 666. It can be seen that the vortex structures are captured very well without fake vortex breakdown or any bulges. The threshold of Ω is always fixed at 0.52, with a physical meaning that vorticity overtakes deformation. Although after a number of adjustments $Q = 0.005$ and $\lambda_2 = -0.005$ can roughly capture the similar structures, their physical meanings are never clear.

3.1.5 Comparison at a Late Time Step

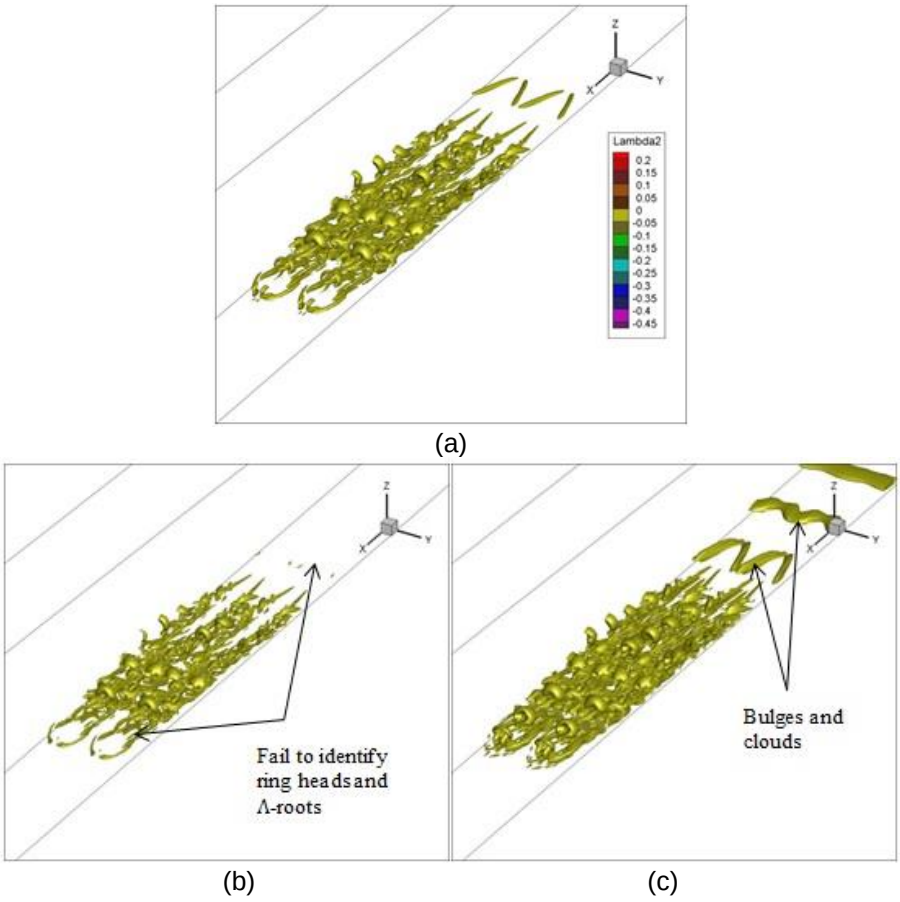

(a)

(b) (c)

Figure 3-9 Iso-surfaces of (a) $\lambda_2 = -0.005$ (b) $\lambda_2 = -0.01$ (c) $\lambda_2 = -0.001$

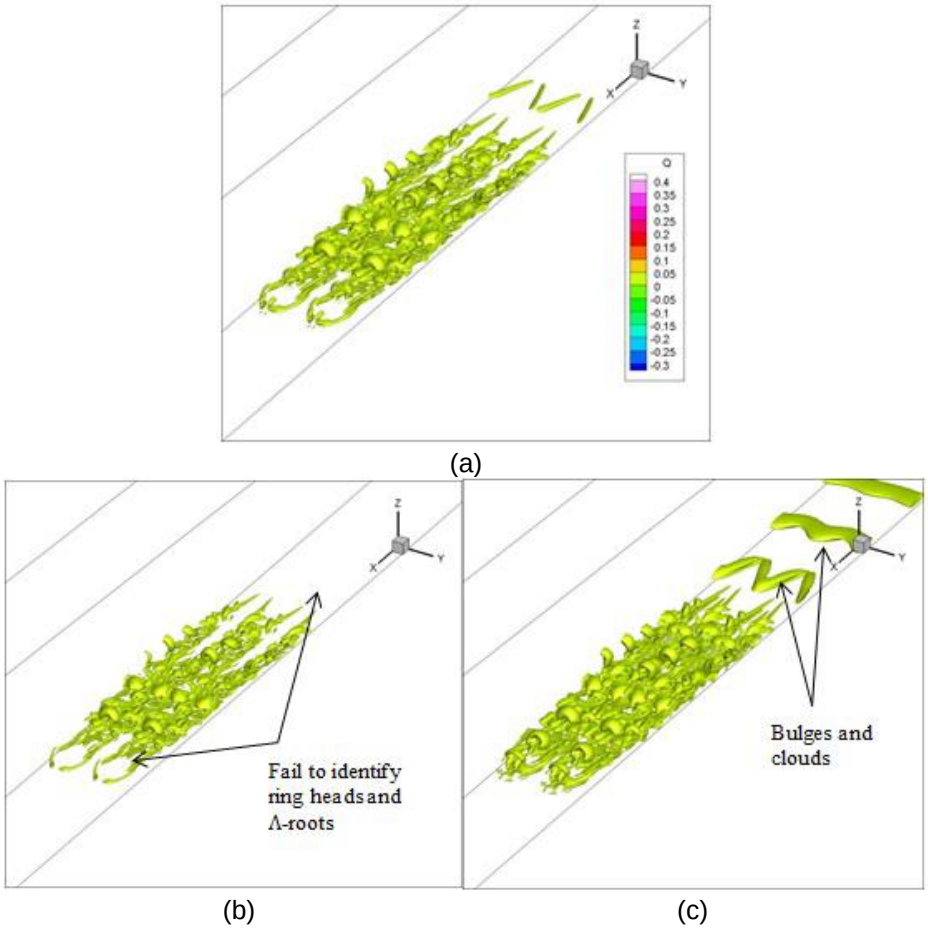

(a)

(b) (c)

Figure 3-10 Iso-surfaces of (a) $Q = 0.005$ (b) $Q = 0.01$ (c) $Q = 0.001$

Now we look at these three vortex identification methods for late boundary layer transition at a late time step t = 808 when the vortices are fully developed. Figure 3-9 gives the vortex structure at $\lambda_2 = -0.005$, $\lambda_2 = -0.01$ and $\lambda_2 = -0.001$ at the same time step. Figure 3-10 gives the vortex iso-surfaces at $Q = 0.005$, $Q = 0.01$ and $Q = 0.001$.

Again there is almost no difference between the visualization by the λ_2 and Q methods. The thresholds in parts (b) of Figures 3-9 and 3-10 do not capture the whole vortex structure because they fail to identify the downstream ring heads and upstream Λ-roots, meaning the weaker vortices are lost in the visualization. On the other hand, in

parts (c) we find extra bulges and clouds which should not be part of the vortex structure. In addition, there are so many vortex layers in parts (c) that smear the main structure. After a lot of adjustments, the parts (a) give us relatively clear pictures. It is argued that Q represents the balance between the strain rate and rotation rate of the fluid element, while λ_2 denotes the pressure minimum in a plane perpendicular to the vortex axis. But what do $Q = 0.005$ and $\lambda_2 = -0.005$ mean? No one can answer this question. The λ_2 and Q methods both suffer from a lack of physical meaning for their values.

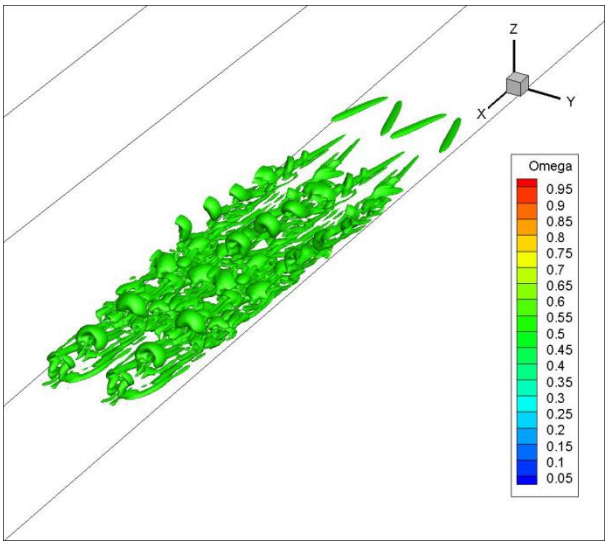

Figure 3-11 Iso-surface of $\Omega = 0.52$

The Omega method gives an innovative mathematical definition of vortex. The iso-surface of $\Omega = 0.52$ can always capture the accurate vortex structure as shown in Figure 3-11. The main structure is visualized very clearly and there are no bulges or clouds. Both strong and weak vortices can be captured simultaneously by the Omega method.

3.2 Vortical Structures behind Micro Vortex Generator

3.2.1 Case Setup

The governing equations are non-dimensional Navier-Stokes equations in conservative forms which are displayed as follows:

$$\frac{\partial Q}{\partial t}+\frac{\partial E}{\partial x}+\frac{\partial F}{\partial y}+\frac{\partial G}{\partial z}=\frac{\partial E_v}{\partial x}+\frac{\partial F_v}{\partial y}+\frac{\partial G_v}{\partial z},$$

where $Q=\begin{pmatrix}\rho\\ \rho u\\ \rho v\\ \rho w\\ e\end{pmatrix}, E=\begin{pmatrix}\rho u\\ \rho u^2+p\\ \rho uv\\ \rho uw\\ (e+p)u\end{pmatrix}, F=\begin{pmatrix}\rho v\\ \rho vu\\ \rho v^2+p\\ \rho vw\\ (e+p)v\end{pmatrix}, G=\begin{pmatrix}\rho w\\ \rho wu\\ \rho wv\\ \rho w^2+p\\ (e+p)w\end{pmatrix},$

$$E_v=\frac{1}{\mathrm{Re}}\begin{pmatrix}0\\ \tau_{xx}\\ \tau_{xy}\\ \tau_{xz}\\ u\tau_{xx}+v\tau_{xy}+w\tau_{xx}+q_x\end{pmatrix}, F_v=\frac{1}{Re}\begin{pmatrix}0\\ \tau_{yx}\\ \tau_{yy}\\ \tau_{yz}\\ u\tau_{yx}+v\tau_{yy}+w\tau_{yz}+q_y\end{pmatrix},$$

$$G_v=\frac{1}{\mathrm{Re}}\begin{pmatrix}0\\ \tau_{zx}\\ \tau_{zy}\\ \tau_{zz}\\ u\tau_{zx}+v\tau_{zy}+w\tau_{zz}+q_z\end{pmatrix},$$

$$e=\frac{p}{\gamma-1}+\frac{1}{2}\rho(u^2+v^2+w^2), p=\frac{\rho T}{\gamma M_\infty^2}, q_x=\frac{\mu}{(\gamma-1)M_\infty^2\mathrm{Pr}}\frac{\partial T}{\partial x},$$

$$q_x=\frac{\mu}{(\gamma-1)M_\infty^2\mathrm{Pr}}\frac{\partial T}{\partial y}, q_x=\frac{\mu}{(\gamma-1)M_\infty^2\mathrm{Pr}}\frac{\partial T}{\partial z}, \mathrm{Pr}=0.72,$$

$$\tau=\mu\begin{bmatrix}\frac{4}{3}\frac{\partial u}{\partial x}-\frac{2}{3}(\frac{\partial v}{\partial y}+\frac{\partial w}{\partial z}) & \frac{\partial u}{\partial y}+\frac{\partial v}{\partial x} & \frac{\partial u}{\partial z}+\frac{\partial w}{\partial x}\\ \frac{\partial u}{\partial y}+\frac{\partial v}{\partial x} & \frac{4}{3}\frac{\partial v}{\partial y}-\frac{2}{3}(\frac{\partial w}{\partial z}+\frac{\partial u}{\partial x}) & \frac{\partial v}{\partial z}+\frac{\partial w}{\partial y})\\ \frac{\partial u}{\partial z}+\frac{\partial w}{\partial x} & \frac{\partial v}{\partial z}+\frac{\partial w}{\partial y} & \frac{4}{3}\frac{\partial w}{\partial z}-\frac{2}{3}(\frac{\partial u}{\partial x}+\frac{\partial v}{\partial y})\end{bmatrix}.$$

The viscous coefficient is given by Sutherland's equation:

$$\mu=T^{3/2}\frac{1+C}{T+C}, \qquad C=\frac{110.4}{T_\infty}.$$

The simulation is performed in a computational domain which contains arbitrary orthogonal curvilinear coordinates. Considering the grid transformation

$$\xi=\xi(x,y,z), \eta=\eta(x,y,z), \zeta=\zeta(x,y,z),$$

the Navier-Stokes' equations can be transformed to the system with generalized coordinates:

$$\frac{\partial \hat{Q}}{\partial \tau}+\frac{\partial \hat{E}}{\partial \xi}+\frac{\partial \hat{F}}{\partial \eta}+\frac{\partial \hat{G}}{\partial \zeta}=\frac{\partial \hat{E}_v}{\partial \xi}+\frac{\partial \hat{F}_v}{\partial \eta}+\frac{\partial \hat{G}_v}{\partial \zeta},$$

where $\hat{Q}=J^{-1}Q$ and

$$\hat{E}=J^{-1}\left(\xi_x E+\xi_y F+\xi_z G\right),\hat{F}=J^{-1}\left(\eta_x E+\eta_y F+\eta_z G\right),\hat{G}=J^{-1}\left(\zeta_x E+\zeta_y F+\zeta_z G\right),$$

$$\hat{E}_v=J^{-1}\left(\xi_x E_v+\xi_y F_v+\xi_z G_v\right),\hat{F}_v=J^{-1}\left(\eta_x E_v+\eta_y F_v+\eta_z G_v\right),\hat{F}_v=J^{-1}\left(\zeta_x E_v+\zeta_y F_v+\zeta_z G_v\right),$$

$$J^{-1}=\det\left(\frac{\partial(x,y,z)}{\partial(\xi,\eta,\zeta)}\right),\xi_x=J\left(y_\eta z_\zeta-z_\eta y_\zeta\right),\text{etc.}$$

MVG (Micro Vortex Generator) is a low-profile passive control device designed for the boundary layer flow control. The computation domain is given in Figure 3-12, where δ_0 is the boundary layer thickness. The height of the MVG h is assumed to be $\delta_0/2$. Flows around MVG are studied with the trailing edge declining angle 70° and the compression angle 24°.

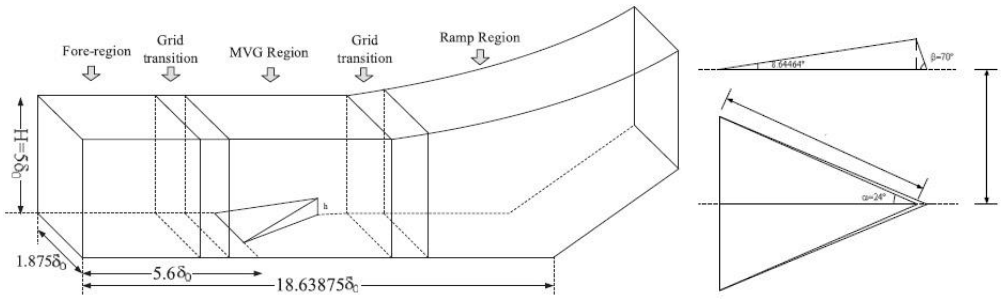

Figure 3-12 The computational domain of the MVG case

Because the singularity of the geometry, it is difficult to use one technique to generate the whole grid system. A general grid partition technique is used in the grid generation. As shown in Figure 3-12, three regions are divided: the ramp region, the MVG region, and the fore-region. Between each two regions, there is a grid transition buffer zone. Because of the symmetry of the grid distribution, only half of the grids need

to be generated. The grid number for the whole system is $\mathrm{n}_{\mathrm{streamwise}} \times \mathrm{n}_{\mathrm{spanwise}} \times \mathrm{n}_{\mathrm{normal}}$ = 1600 × 128 × 192.

3.2.2 Numerical Methods

The implicitly implemented LES method and the fifth order bandwidth-optimized WENO scheme are used to solve the unfiltered form of the Navier-Stokes equations at Mach = 2.5 and Re = 5760. Considering the one-dimensional hyperbolic equation

$$\frac{\partial u}{\partial t} + \frac{\partial f(u)}{x} = 0,$$

the semi-discretized equation can be written as

$$\left(\frac{\partial u}{\partial t}\right)_j = -\frac{h_{j+\frac{1}{2}} - h_{j-\frac{1}{2}}}{\Delta x}.$$

To reduce the dissipation, the less dissipative Steger-Warming flux splitting method is used instead of the dissipative Lax-Friedrich splitting method. For the positive flux, the three upwind-biased schemes can be expressed as

$$h_1^{+\prime} = \frac{1}{3} f_{j-2} - \frac{7}{6} f_{j-1} + \frac{11}{6} f_j,$$

$$h_2^{+\prime} = -\frac{1}{6} f_{j-1} + \frac{1}{3} f_j + \frac{5}{6} f_{j+1},$$

$$h_3^{+\prime} = \frac{1}{3} f_j + \frac{5}{6} f_{j+1} - \frac{1}{6} f_{j+2}.$$

The final nonlinear weighted scheme is

$$h_{j+1/2}^{+} = w_1 h_1^{+\prime} + w_2 h_2^{+\prime} + w_3 h_3^{+\prime},$$

where the WENO weights w_i and the smoothness indicators IS_i are given by

$$w_i = \frac{b_i}{b_1 + b_2 + b_3}, b_i = \frac{a_i}{(IS_i + \varepsilon)^2}, (a_1, a_2, a_3) = (0.1, 0.6, 0.3),$$

$$IS_1 = \frac{13}{12}\left(f_{j-2} - 2f_{j-1} + f_j\right)^2 + \frac{1}{4}\left(f_{j-2} - 4f_{j-1} + 3f_j\right)^2,$$

$$IS_2 = \frac{13}{12}\left(f_{j-1} - 2f_j + f_{j+1}\right)^2 + \frac{1}{4}\left(f_{j-1} - f_{j+1}\right)^2,$$

$$IS_3 = \frac{13}{12}\left(f_j - 2f_{j+1} + f_{j+2}\right)^2 + \frac{1}{4}\left(3f_j - 4f_{j+1} + f_{j+2}\right)^2.$$

The scheme for the negative flux $h^-_{j+1/2}$ has a similar form to $h^+_{j+1/2}$ at point $x_{j+1/2}$.

The periodic boundary conditions are applied on the spanwise direction. The adiabatic, zero-pressure gradient and no-slip conditions are enforced on the wall boundary. On the far field and outflow boundaries, the non-reflecting boundary conditions are adopted. The fully developed turbulent inflow boundary conditions are generated by 20,000 turbulent profiles from our DNS simulation.

As for the time marching, the explicit third order TVD Runge-Kutta scheme is adopted for temporal terms in the Navier-Stokes equations:

$$u^{(1)} = u^n + \Delta t L(u^n),$$

$$u^{(2)} = \frac{3}{4}u^n + \frac{1}{4}u^{(1)} + \frac{1}{4}\Delta t L\left(u^{(1)}\right),$$

$$u^{n+1} = \frac{1}{3}u^n + \frac{2}{3}u^{(2)} + \frac{2}{3}\Delta t L\left(u^{(2)}\right),$$

where L is the differential operator which denotes the spatial derivatives, i.e.,

$$L(u) = -\frac{\partial E(u)}{\partial x} - \frac{\partial F(u)}{\partial y} - \frac{\partial G(u)}{\partial z} + \frac{\partial E_v(u)}{\partial x} + \frac{\partial F_v(u)}{\partial y} + \frac{\partial G_v(u)}{\partial z}.$$

3.2.3 Code Validation

Figure 3-13 shows the inlet velocity profile in log-coordinates, which agrees well with the analytical profile from Guarini et al. (2000) on the same cross section.

According to our analysis, a dynamic vortex model is given in Figure 3-14 left. The dominant vortex near the MVG is the primary vortex underneath which there are two first secondary counter-rotating vortices. These vortices will merge into the primary vortex when they propagate downstream, while the new secondary vortex will be generated

under the primary vortex and travel with the speed of sound. This dynamic vortex model is mostly confirmed by the experimental work of Saad et al. (2012) in Figure 3-14 right.

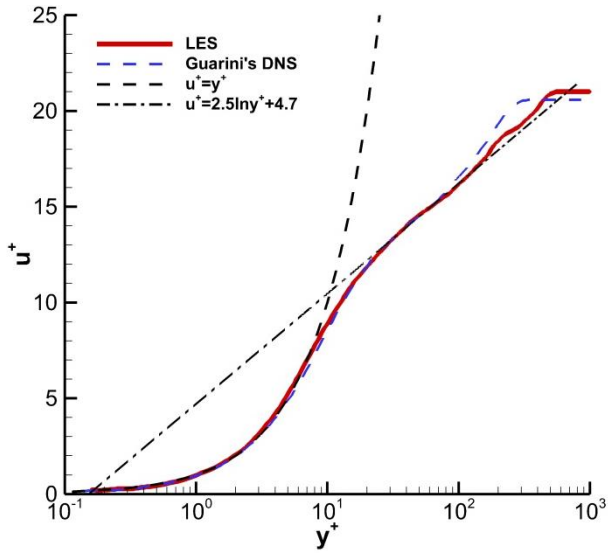

Figure 3-13 Inflow boundary layer velocity profile compared with Guarini et al.

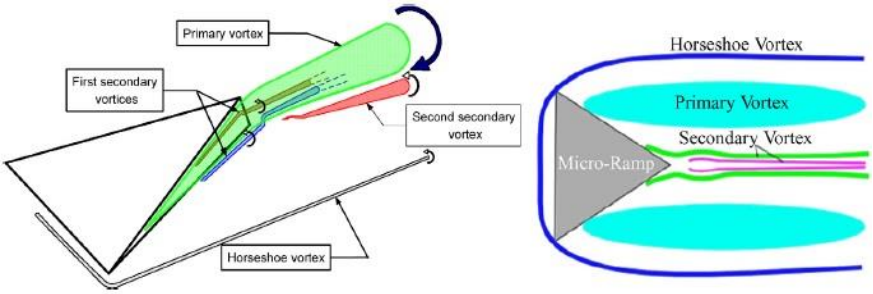

Figure 3-14 The MVG vortex model (left) confirmed by Saad et al. (right)

Our numerical discovery of the vortex ring structure is confirmed by the 3-D particle image velocimetry (PIV) experiment conducted by Sun et al. (2012) at Delft University. Comparing the two results in Figure 3-15, we can find the similar distributions of streamwise and spanwise vorticity components, which prove the existence of the ring structures.

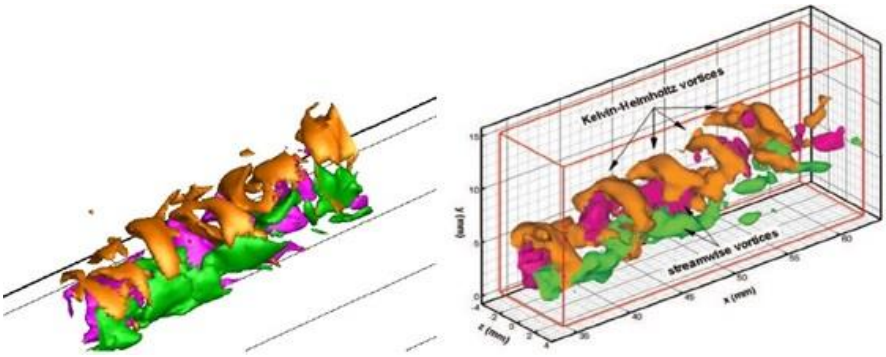

Figure 3-15 Distribution of streamwise and spanwise vorticity from our LES (left) and from experiment by Sun et al. (right)

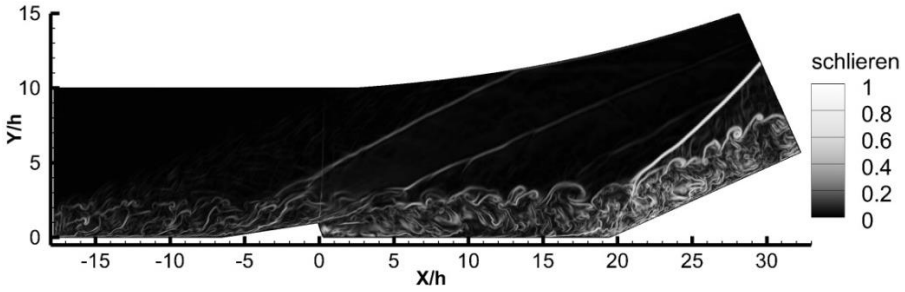

(a)

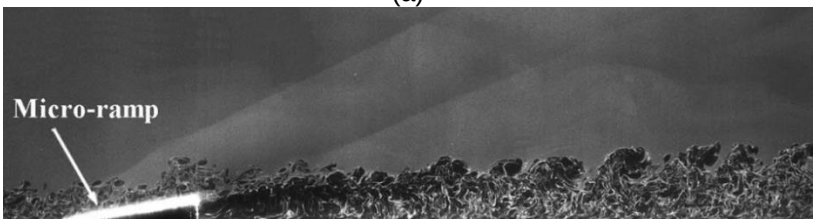

(b)

Figure 3-16 Wake vortical structures behind MVG (a) the schlieren on the central plane given by our LES results (b) the NPLS image of Wang et al.

Figure 3-16(a) shows the schlieren of the turbulent compression ramp flow with MVG on the central plane based on our LES result. Figure 3-16(b) is the NPLS image of wake structures behind MVG presented by experimental result of Wang et al. (2012), obtained from the supersonic channel flow at Mach = 2.7 and Re = 5845. Compared with the experiment result, some typical structures around MVG can be observed in the LES

results, such as the first and second shock wave at the leading and trailing edge of MVG, and a chain of ring-like vortices behind the MVG.

Figure 3-17 gives a qualitative comparison with the experiment done by Babinsky et al. (2009) in the time and spanwise averaged velocity profile behind the MVG. An agreement is achieved.

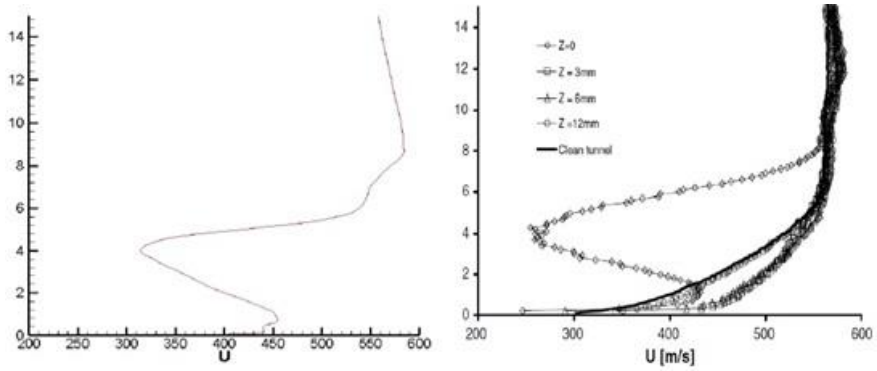

Figure 3-17 Comparison of time averaged velocity profile of LES (left) with experiment by Babinsky et al. (right)

3.2.4 Comparison

The three visualization methods are illustrated and compared at the same time step. Figure 3-18 shows the vortex iso-surfaces of $\lambda_2 = -0.001$, $\lambda_2 = -0.01$ and $\lambda_2 = -0.0001$ respectively. We can see that the ring-like structures are identified well in part (a). A chain of vortex rings are generated after the trailing edge of the MVG and propagate further downstream. The mechanism for the vortex ring generation could be the Kelvin-Helmholtz type instability. The loss of the stability on the shear layer would result in the roll-up of the vortices, which appear as ring-like structures in the 3-D view. A larger magnitude of λ_2 in part (b) leads to the loss of the main structures and may give the wrong impression of vortex breakdown. A smaller magnitude in part (c) will cause a chaos of the visualization which prevents us from recognizing the ring-like vortices.

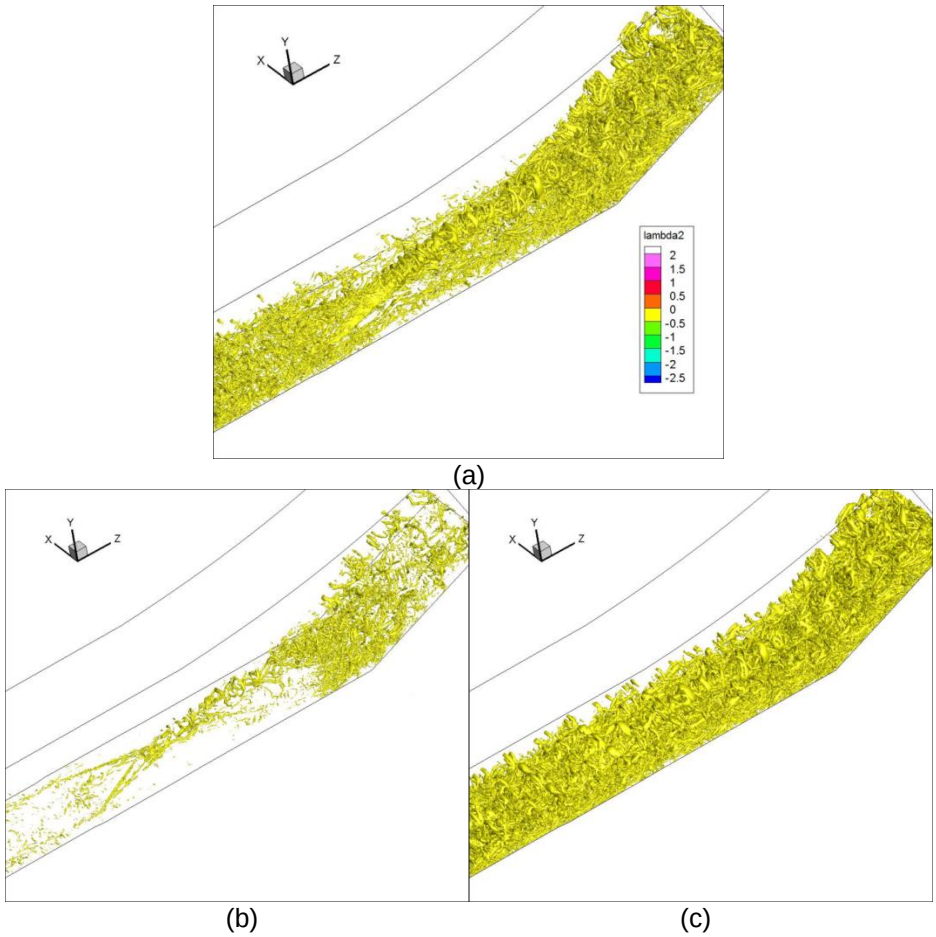

Figure 3-18 Iso-surfaces of (a) $\lambda_2 = -0.001$ (b) $\lambda_2 = -0.01$ (c) $\lambda_2 = -0.0001$

If one imitates the transition case and selects $Q = 0.001$ to identify the ring-like vortices, the structures in Figure 3-19 will be obtained. Everything becomes chaotic and some noises appear on the top of the vortex structures. We have to put some effort to adjust the threshold for the Q-criterion. We find a proper threshold which gives similar visualization to Figure 3-20(a). Figure 3-20 shows the iso-surfaces of $Q = 1$, $Q = 10$ and $Q = 0.1$ respectively. Again the part (a) provides the most accurate vortex structures. A larger magnitude of the Q value fails to identify the accurate vortex structure, while a smaller magnitude will make the vortices indistinguishable from one another.

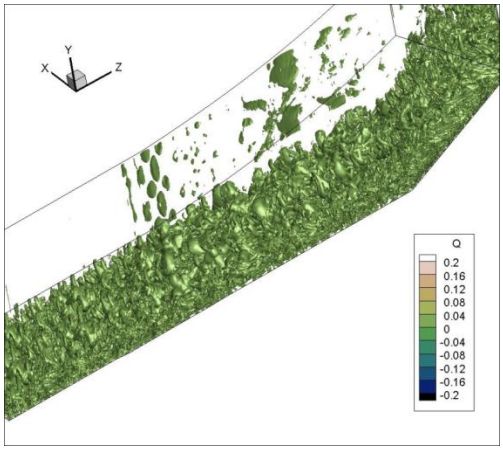

Figure 3-19 Improper vortical structures given by iso-surface of $Q = 0.001$

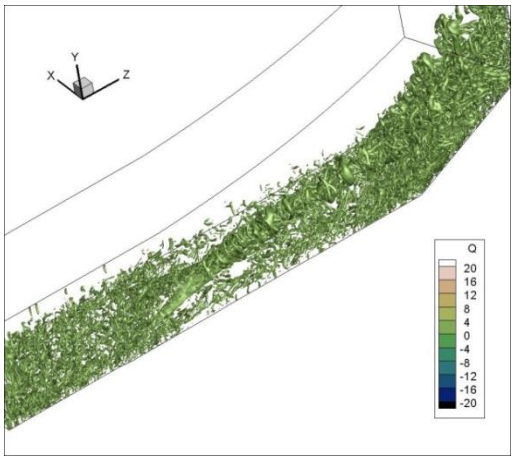

(a)

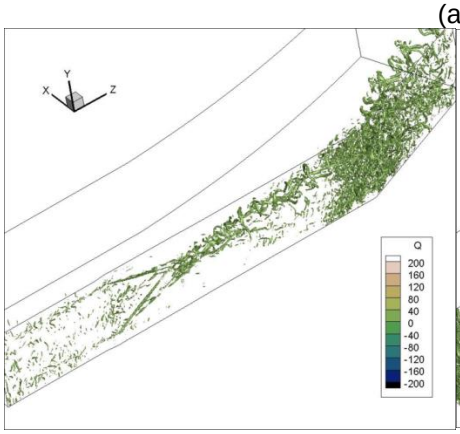

(b)

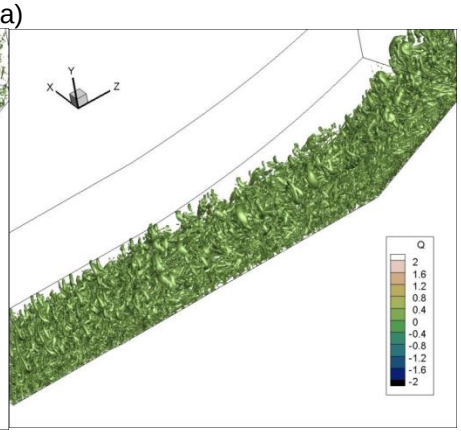

(c)

Figure 3-20 Iso-surfaces of (a) $Q = 1$ (b) $Q = 10$ (c) $Q = 0.1$

Sometimes it is painful to adjust the thresholds for the λ_2 and Q methods case by case and time by time. Even though a proper threshold is chosen, there is no universal criterion to tell whether such a threshold is correct or not. Therefore it is quite necessary to introduce a new vortex identification method which can visualize the vortex structures accurately and universally. The Omega method is proposed under such background.

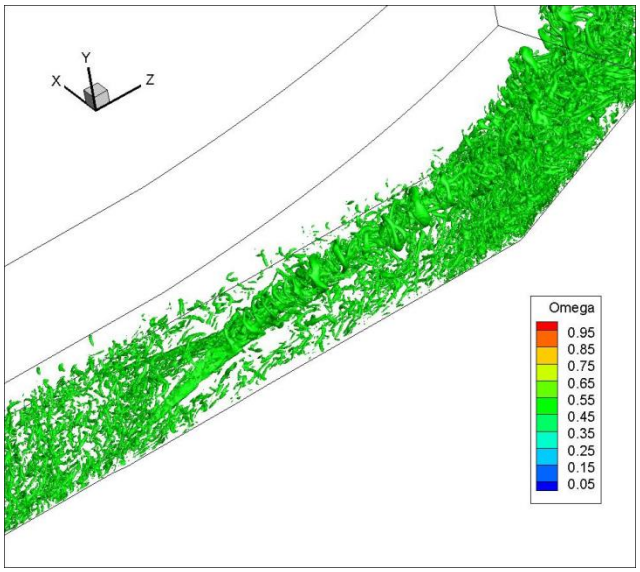

Figure 3-21 Iso-surface of $\Omega = 0.52$

Figure 3-21 gives the vortex iso-surface at the fixed Ω value 0.52. The ring-like structures are captured clearly including the weak vortices beneath the chain of vortex rings. It should be noticed that the MVG case is quite different from the boundary layer transition in many aspects such as flow speed, compressibility and other conditions. Despite the differences, the Omega method still well captures the ring-like structures at the fixed threshold $\Omega = 0.52$.

A fixed threshold and thus no need to adjust is a major advantage of the Omega method over the other two methods, which makes Ω method the most effective and efficient tool in vortex identification.

3.3 Results from Other Users

3.3.1 Vortices in Turbine Tip Clearance

For a long time, Z. Zou, F. Shao and W. Zhang at Beihang University, China, used the Q method to visualize the vortex structure but always missed weak vortices. The Omega method works very well without adjusting any threshold as shown in Figure 3-22(c).

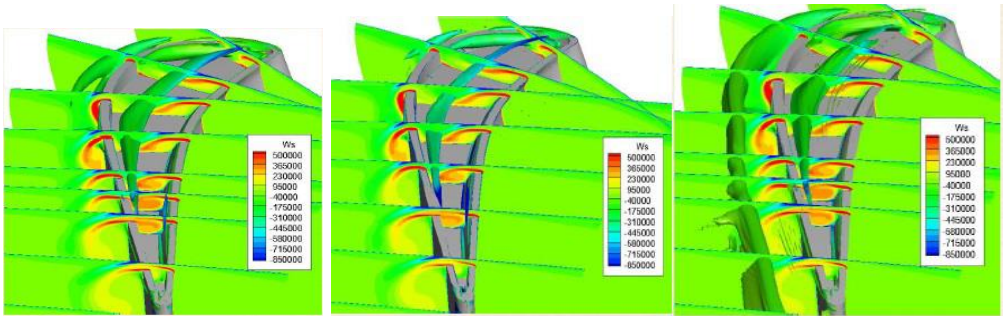

(a) (b) (c)

Figure 3-22 Iso-surfaces of (a) $Q = 1 \times 10^9$ (b) $Q = 1 \times 10^{10}$ (c) $\Omega = 0.52$

3.3.2 Transition of a Vortex Ring

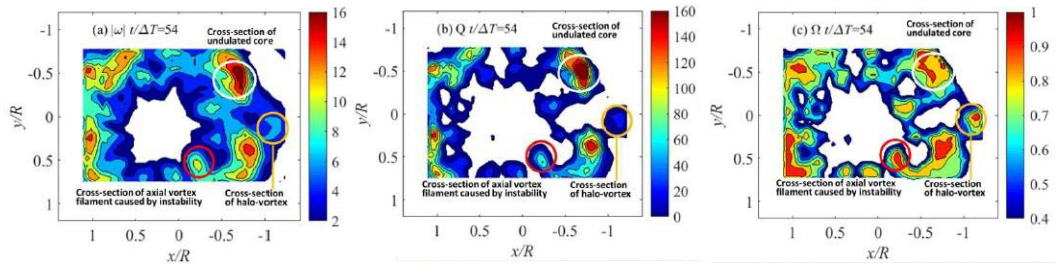

(a) (b) (c)

Figure 3-23 The horizontal cross-section through the center of vortex ring represented by (a) vorticity magnitude (b) Q method (c) Ω-method

Figure 3-23 is the joint work from researchers at London City University, UK, and Freiberg Technical University, Germany. Using the Ω method as the vortex identification criterion, the three types of vortex with different strength, namely the ring core, axial

filament produced by azimuthal instability and the halo-vortex, are visualized simultaneously as shown in Figure 3-22(c).

3.3.3 Visualization of Spatially Developing Vortices

Figure 3-24 is contributed by Qin Li at Chinese Aerodynamics Development Center, Mianyang, Sichuan, China. The weak vortices are completely lost using Q method (left), while the Omega method can capture both strong and weak vortices (right).

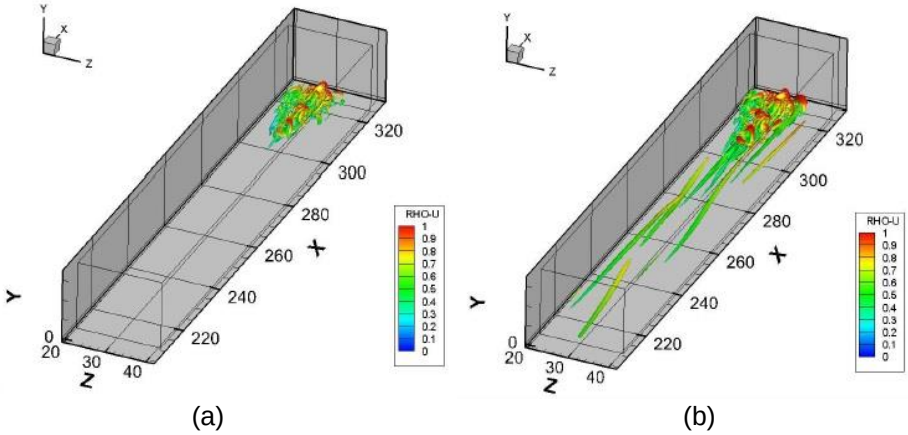

(a) (b)

Figure 3-24 Iso-surfaces of (a) $Q = 0.025$ (b) $\Omega = 0.52$

3.4 Advantages of Ω Method

From the above comparisons, we find the following advantages of the Omega method over the traditional λ_2 method and Q method:

1) The Omega method gives a mathematical definition that vortex is a region where $\Omega > 0.5$. It has a clear physical meaning that vorticity overtakes deformation. But no one can explain what $Q = 0.005$ or $\lambda_2 = -0.005$ means.

2) Ω = 0.52 always well captures the vortex surface. The reason we select Ω = 0.52 is empirically this threshold works for all cases we studied.

3) There is no need to select a “proper threshold” case by case, time by time or even region by region for the same case.

4) The Omega method can capture both strong vortex and weak vortex without much adjustment.

These features of the Omega vortex identification method will be valuable and useful for the study of turbulence physics and many other vortex dominant flows in science and engineering.

Chapter 4

Application on Shock Wave Vortex Ring Interaction

4.1 Shock Boundary Layer Interaction

Shock wave boundary layer interactions (SBLIs) occur when a shock wave and a boundary layer converge in supersonic flows. When the flow crosses a shock wave, it experiences a discontinuous velocity decrease, an abrupt increase in pressure, a rise in flow temperature, and a rise in entropy. In any SBLI, the shock imposes an intense adverse pressure gradient, which significantly distorts the boundary layer velocity profile. This produces an increase in the displacement effect that influences the neighboring inviscid flow. These consequences are exacerbated when the shock is strong enough to separate the boundary layer, which can lead to dramatic changes in the entire flow field structure with the formation of intense vortices or complex shock patterns.

Shock induced separation may trigger large-scale unsteadiness, leading to buffeting on wings, buzz for air-intakes, or unsteady side loads in nozzles. They could act as strong aerodynamic loads, and lead to heavy drag rise, acoustic noises and even structure damage. In hypersonic flight, SBLIs can be disastrous because at high Mach numbers, they have the potential to cause intense localized heating that can be severe enough to destroy a vehicle. Because of their significance for many practical applications, SBLIs have been the focus of numerous studies for several decades.

A detrimental consequence of SBLI is the occurrence of flow unsteadiness, which can be of high intensity when the shock is strong enough to induce separation. Such unsteadiness can occur at low frequencies when associated with turbulent fluctuations and separation bubble instabilities. The relationship between the upstream boundary layer and the low-frequency, largescale unsteadiness of the separated flow in a compression ramp interaction investigated by Ganapathisubramani et al. (2007, 2009)

indicated that the low-frequency unsteadiness of the separation region/shock foot could be explained by a turbulent mechanism that includes high and low speed regions in the upstream boundary layer, which means the incoming boundary layer is at the origin of the low-frequency unsteadiness. In recent years, a series of studies on the statistical relation between the low-frequency shock motion and the upstream and downstream flow was proposed by Priebe and Martin (2012). They held the view that the shock motion is related to the separation bubble breathing and the separated shear layer flapping. In addition, the inherent instability in the downstream separated flow is the physical origin of the low-frequency unsteadiness. Wu and Martin (2008) investigated the shock motion based on their direct numerical simulation data of a Mach 2.9, 24° compression ramp configuration. They believed that the spanwise mean separation point undergoes a low-frequency motion and is highly correlated with the shock motion, which indicated that the low-frequency shock unsteadiness is affected by the downstream flow. Clemens et al. (2009) and Souverein et al. (2010) believed that both upstream and downstream effects existed in the low-frequency unsteadiness and downstream effects dominated for fully separated flow, whereas upstream effects became dominant for mild interactions.

Because it is often difficult to avoid detrimental SBLIs occurring within a flow, the target of the control techniques is mainly to either reduce shock induced separation or stabilize the shock when it occurs in naturally unsteady configurations. The upstream influence of the shock and the resistance of a turbulent boundary layer to separation depend mainly on the momentum. Thus, one way to limit the shock's effect is to increase the boundary layer momentum prior to interaction with shock, which can be done by appropriate boundary layer manipulation techniques, such as mass injection through one or several slots located upstream of the shock region, removal of the low-speed part of the boundary layer by applying strong suction through a slot located within the interaction

region, and use of vortex generators upstream of the shock, which transfer momentum from the outer high-speed flow thereby enhancing resistance to an adverse pressure gradient.

Micro vortex generator (MVG), which is widely used in SBLI control to decrease the adverse effects of separation, is a kind of low-profile passive control device with a lower height (less than half of the boundary layer thickness) compared with conventional vortex generators. It receives great research interests because of its remarkable capacity of alleviating flow separation while carrying much lower drag penalty, which is encountered in many aerospace applications, such as supersonic inlets, propulsion-wing, etc. As a kind of miniature and passive device, MVG has clear advantages in low profile drag, lack of intrusiveness, and robustness. Therefore, many efforts for experimental and computational investigations have been devoted to demonstrate its effectiveness and the working mechanism in the separation control.

Most researchers believe that a pair of streamwise vortices generated by MVG is dominant in separation control, which can generate energy and momentum exchange between the high-speed freestream and the lower-momentum boundary layer through the up-wash and down-wash motions, and finally modify the pressure distribution of the boundary layer and make it less likely to separate. Because of the supersonic boundary layer inflow, it is expected that MVG will lead to strong disturbances like shock waves. Experiment was performed by Holden and Babinsky (2007) in a supersonic wind tunnel to investigate the effect of the wedge-shaped and vane-type sub-boundary layer vortex generators (SBVGs) placed upstream of a normal shock turbulent boundary layer interaction at Mach = 1.5 and Re = 28×10^6. The results showed that both two types of SBVGs could generate two pairs of counter-rotating vortices to reduce the size of the shock-induced separation. Especially the vane-type SBVGs could eliminate the

separation entirely due to the generation of more widely spaced primary vortices. Under the experimental conditions given by Babinsky, Ghosh et al. (2008) simulated the effects of MVGs in controlling oblique shock and turbulent boundary layer interactions by Reynolds averaged Navier–Stokes (RANS) and RANS/LES models. They concluded that the major effect of the micro vortex generator array is to induce a pair of counter-rotating longitudinal vortices, which force higher momentum fluid toward the surface and energize the lower momentum boundary layer.

Although numerous experimental and numerical studies for SBLI control by MVG were carried out and MVG was proved to be the efficient device to delay the separation induced by SBLI, its control mechanism of vortex motions was still not clear until Li and Liu (2010) first discovered the large scale vortex rings behind MVG in a supersonic compression ramp flow at Mach = 2.5, Re = 1440 by the monotone integrated LES with fifth-order WENO scheme. A pair of counter-rotating streamwise vortices and the underneath attached secondary ones are considered to be the mechanism of the flow control. The downwash by the vortices will bring high speed momentum to the boundary layer, which is favorable to resistance of the adverse gradient of the pressure.

The shock ring interaction controlled by the MVG poses great challenges for numerical flow simulations. Lee et al. (2010) showed that Reynolds-averaged Navier-Stokes computations are not very well suited for these kinds of problems and deliver results that deviate significantly from experimental data. Large Eddy Simulations on the other hand produce results that are much closer to the experimental evidence. In the following sections, we will use LES to investigate the three dimensional shock ring interaction for the MVG controlled supersonic ramp flow by tracking large-scale vortex rings during the process of passing through the shock. A new mechanism on the SBLI control by MVG was discovered as associated with a chain of vortex rings, which strongly

interact with the shock and play an important role in the separation zone reduction. These vortex rings could be a dominant factor of the mechanisms of MVG in the control of shock turbulent boundary layer interaction. We concentrate on the process of the shock wave and vortex ring interaction, the correlation and frequency coherence between their motions and the locations of the separation bubble. The shock ring interaction can be used to explain the source of the low-frequency unsteadiness and the large-scale pulsations of the separation bubble.

4.2 Investigation on Shock Ring Interaction

A chain of vortex rings are generated from the trailing edge of the MVG as shown in Figure 4-1. These rings propagate further downstream and interact with the impinging shock wave, eventually distorting the structure of the shock wave. Although the shock is badly distorted, the vortex rings are persistent and do not break up during the interaction. In Figure 4-1, the ring structures in green are visualized using the Omega method at the iso-surface of $\Omega = 0.52$, and the shock is identified by the red iso-surface measured by the pressure gradient magnitude.

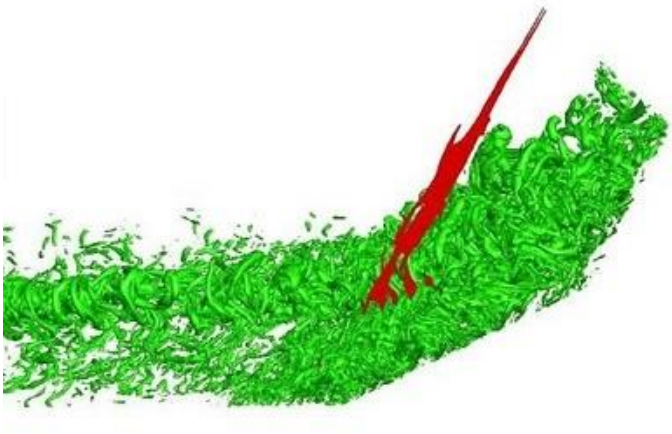

Figure 4-1 Shock ring interaction behind the MVG

To study the flow properties and reveal the mechanism of separated flow unsteadiness, we track one typical vortex ring before, when and after it hits the shock front starting from the time step t = 1800T. We cut off the central plane on which the cross section gives the vortices of the largest scale. The circled red spot represents the ring head being tracked and the black contour lines represent the presence of the shock wave (Figure 4-2). The initial position of the ring head is at approximately (x, y) = (18, 2.5) in the upstream boundary layer.

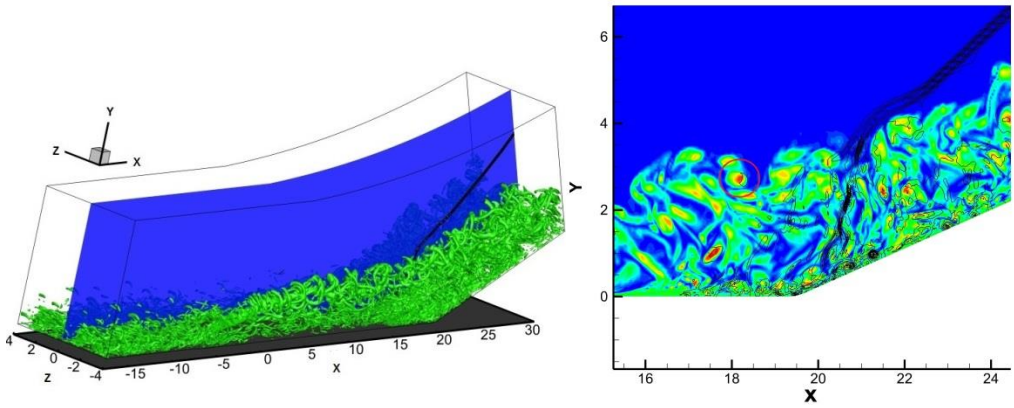

Figure 4-2 The central plane at t = 1800T

4.2.1 Influence on Oblique Shock

Figure 4-3 shows the four critical time steps during the shock ring interaction, from which the role of vortex ring movement on the shock motion is illustrated. The vortex ring hits the shock front at t = 1844T in figure (a). When the ring is passing through the shock, the vortex structure is slightly distorted due to deformation. The vortex ring does not break down after penetrating the strong shock and maintains its original topology very well, which means that, in the three dimensional shock ring interaction, the vortical structure in the shear layer is almost not affected by the shock.

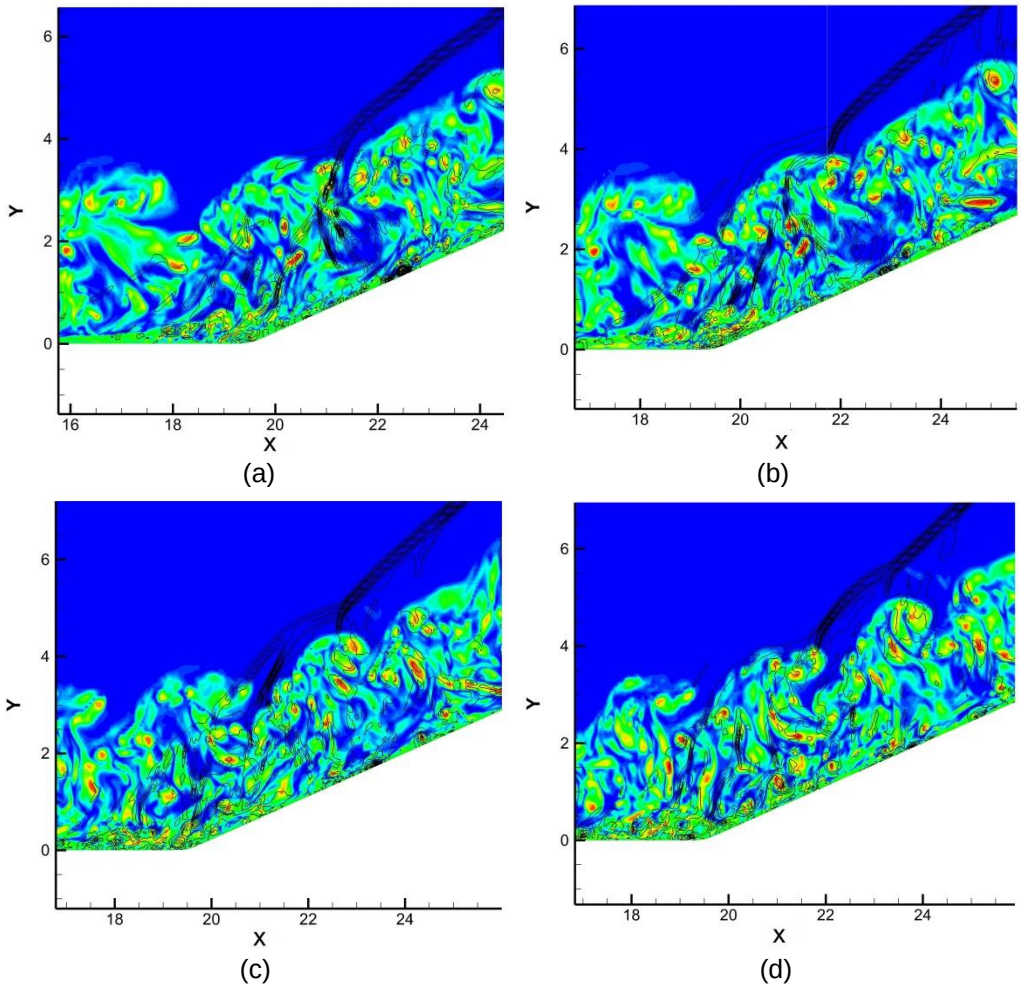

Figure 4-3 Four time steps during the shock ring interaction

(a) t = 1844T (b) t= 1864T (c) t = 1884T (d) t = 1904T

However, the shock begins to get distorted at t = 1864T in figure (b) and soon becomes broken at t = 1884T in figure (c). The reason is that at the very thin shock front the pressure is substantially high. When the vortex rings travel downstream, they carry relative low pressure and interact with the shock. The instantaneous pressure will drop dramatically at the interaction region, which results in the movement of the shock with the rings. A qualitative analysis of the shock intensity change will be given in section 4.2.2.

At a later time step t = 1904T in figure (d), the upper reflection shock recovers quickly after the previous ring leaves, but the lower separation shock keeps getting distorted with the chain of vortex rings coming from the upstream continuously. The propagation of the rings causes the shock foot to sweep back and forth. The outer region of the separation zone looks quite chaotic. As we can see, there are many weak shocks formed around the small scale rings near the wall because of the fast rotation of the rings (around 64000 cycles per second). The shock ring interaction in the downstream may in turn affect the separation bubble dynamics and low-frequency oscillations.

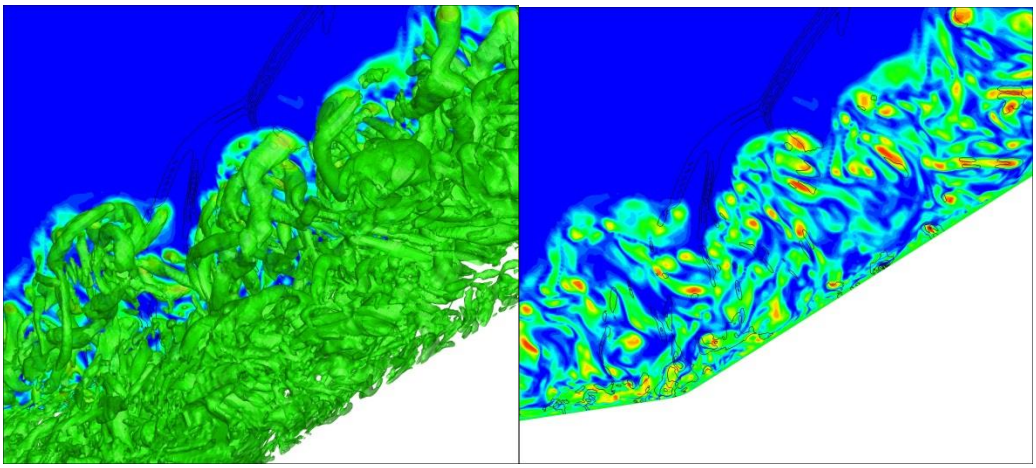

Figure 4-4 The 3D vortical structures at t = 1884T

Figure 4-4 shows the three dimensional vortical structure with its two dimensional counterpart at t = 1884T. The large scale rings are dominant in the outer region of the separation zone and the passage of the upstream rings is directly responsible for the motion of the shock. It is possible that the low-frequency unsteadiness is due to the shock ring interaction. Some statistical analysis is needed to find the correlation between the strength of the rings and the separation shock motion. More information will be given in section 4.3.

4.2.2 Influence on Vortex Ring

We observe the flow properties of the above ring head (circled in Figure 4-2) for 20 time steps starting from t = 1800T. The quantities are recorded for the points of the largest Omega value at which the rotation is the most dominant. Figure 4-5 shows the position of the ring head throughout the interaction. We see that the ring is traveling downstream and rolling up due to the placement of the ramp.

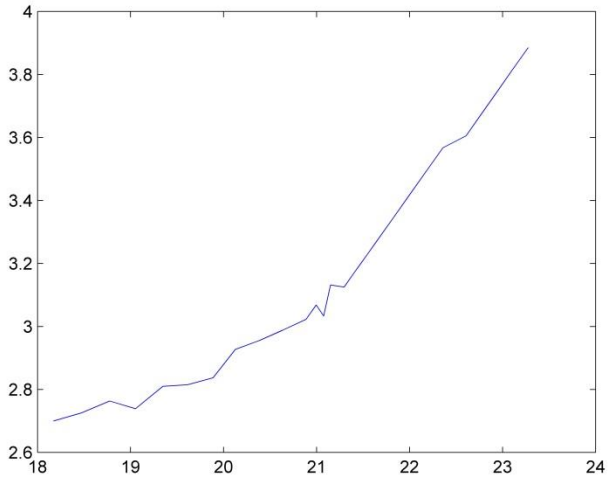

Figure 4-5 The position of the vortex ring

When the flow passes through the shock wave, its properties such as pressure, density, energy, velocity and vorticity will change discontinuously. As the ring travels downstream, its pressure gradient suddenly jumps from 1.5 to 5 at around X = 21 where it meets the shock (Figure 4-6). After it penetrates the shock, its pressure gradient drops quickly. It is interesting that a number of weak shocks are found around the ring behind the strong shock. This is because the ring is rotating very fast with low pressure and can be viewed as a solid body; when the surrounding flows move to the ring, the pressure decreases dramatically thus weak shocks are formed.

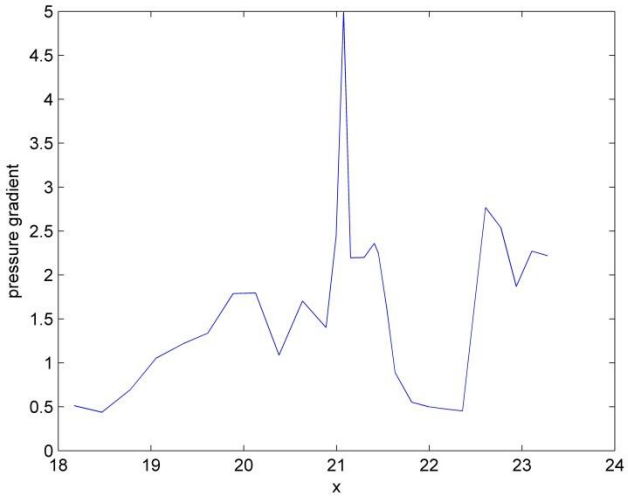

Figure 4-6 The pressure gradient of the vortex ring

Figures 4-7 and 4-8 give the distributions of density and energy of the ring versus streamwise location as time evolves. These two quantities keep increasing due to the heat and energy transport during the shock ring interaction. There is a jump at the position of the shock (X = 21).

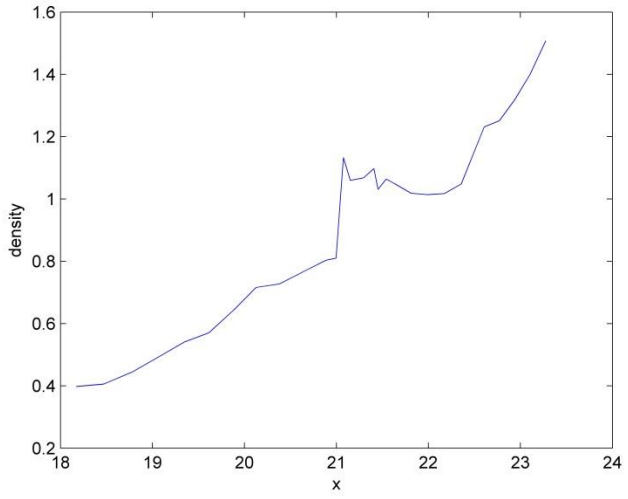

Figure 4-7 The density of the vortex ring

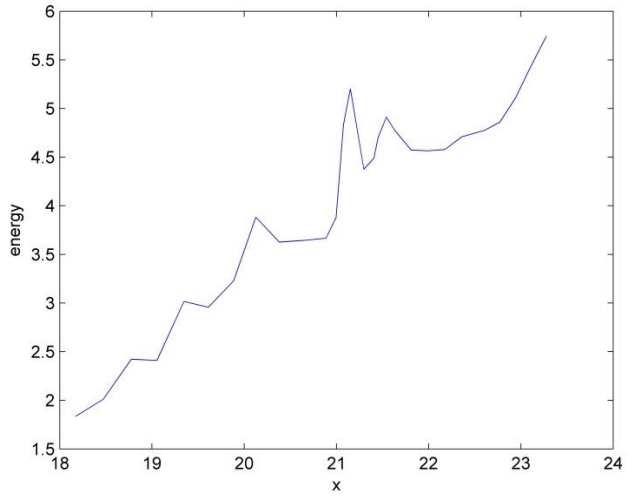

Figure 4-8 The energy of the vortex ring

The velocity profile of the ring during the interaction is plotted in Figure 4-9. The streamwise velocity of the ring head is decreasing throughout the interaction, which means the ring is hold back by the shock. There is a discontinuity at the position of the shock, but the overall movement of the ring is not affected by the interaction with the shock. The increase of the wall normal velocity shows the ring is rolling up gradually.

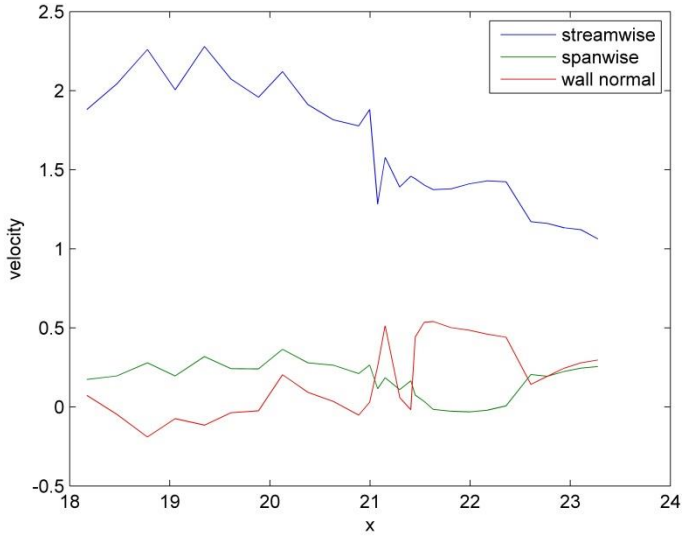

Figure 4-9 The velocity profile of the vortex ring

The vorticity distribution during the interaction is shown in Figure 4-10. The main finding is that the spanwise vorticity is taking the leading role when the ring travels downstream, since the vorticity magnitude basically follows the same track of the spanwise vorticity. Vorticity is related to the average angular velocity of a rotating body. Although the wall normal vorticity increases in time, the spanwise vorticity is dominant as a decreasing trend, indicating that the rotation of the vortex ring is not as fast as before it hits the shock. This fact is further confirmed by the distribution of the Omega value in Figure 4-11. Omega measures the stiffness of the flow. From the definition, larger Omega means vorticity is more dominant. Hence, the decrease of Omega demonstrates that the rotation of the vortex ring is not as strong as before.

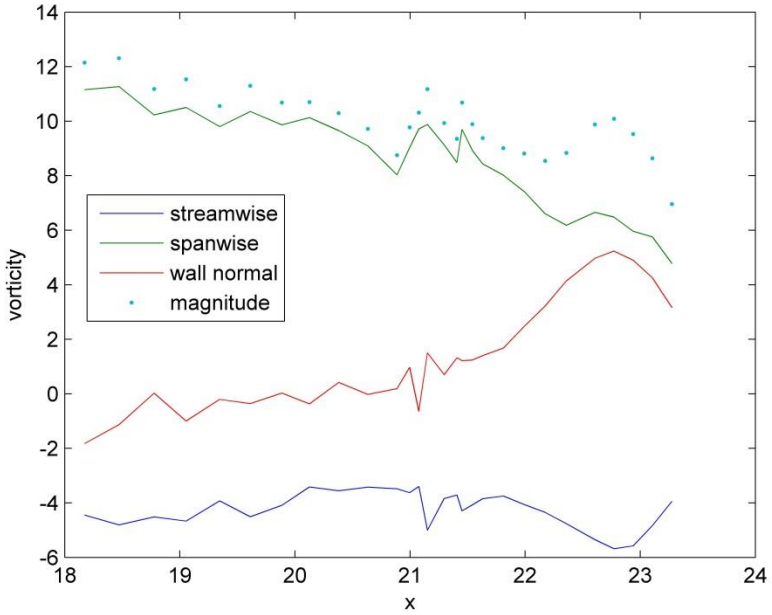

Figure 4-10 The vorticity distribution of the vortex ring

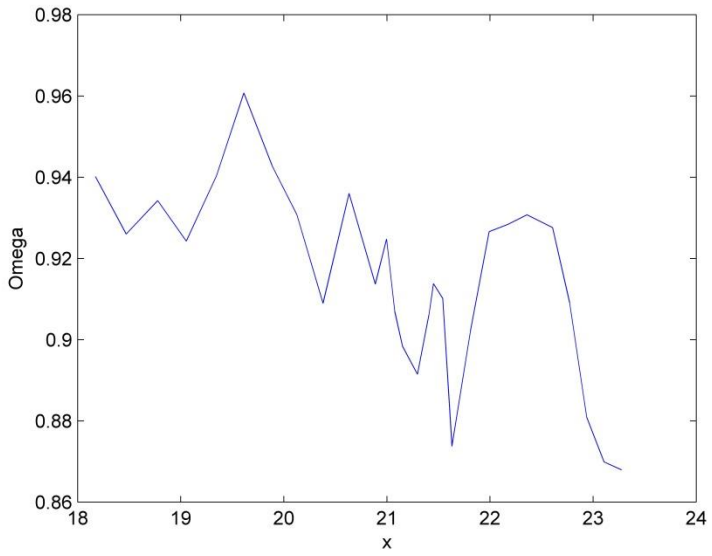

Figure 4-11 Distribution of the Omega value

4.2.3 Influence on Separation Bubble

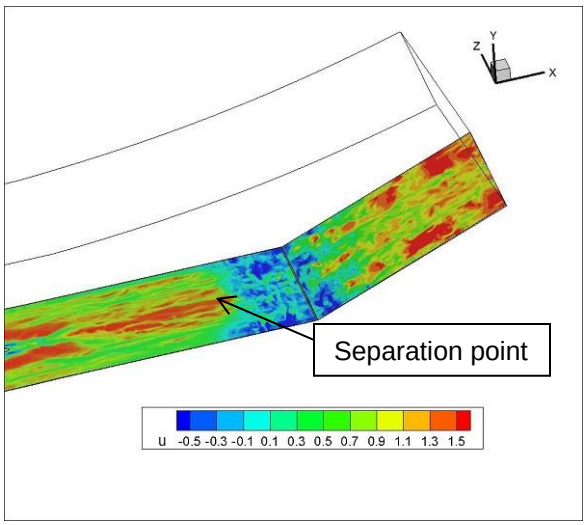

Figure 4-12 The separation zone contoured by the streamwise velocity

Figure 4-12 shows the three dimensional separation zone near the wall and Figure 4-13 shows the streamwise position of the separation point when $\partial u/\partial y = 0$ on the central plane. It is clear that the vortex rings reduce the flow separation in the central

region. The propagation of the rings causes the shock foot to sweep back and forth, which will induce the separation bubble to shrink and grow over time.

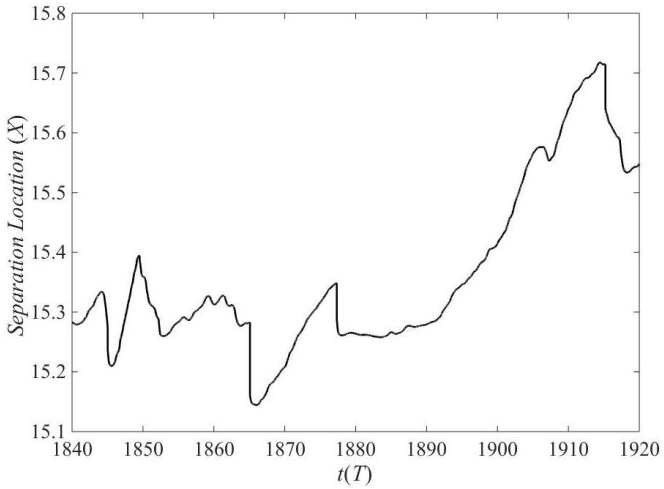

Figure 4-13 Streamwise positon of the separation point on the central plane

As shown in Figure 4-14, at t = 1804T the previous rings have passed the shock and the new rings have not arrived, the separation bubble is shrinking; at t = 1844T the shock is pushed forward by the rings, the bubble is growing.

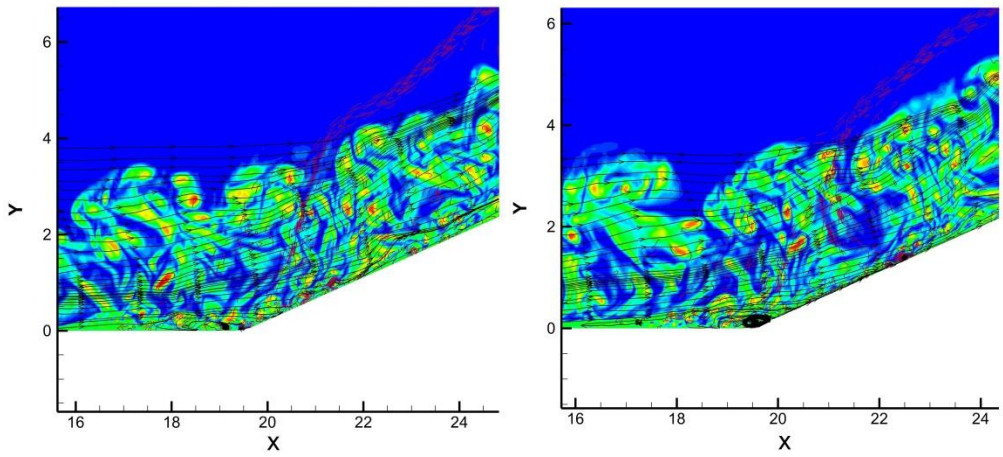

(a) t = 1804T (b) t = 1844T

Figure 4-14 The movement of the separation bubble

4.3 Statistical Analysis

4.3.1 Statistical Correlation between Vortex Rings and Shock Motion

As discussed in section 4.2.1, the reflection shock gets distorted when a vortex ring passes through and recovers after it leaves. As more rings travelling from the incoming boundary layer, the separation shock keeps being distorted and sweeps back and forth. The statistical relation between the movement of vortex rings and the shock motion is investigated.

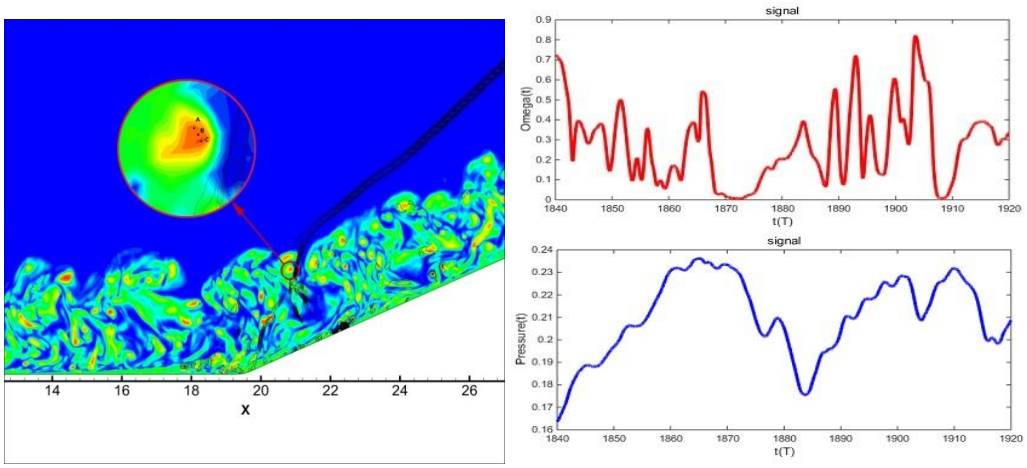

Figure 4-15 The correlation between vortex rings and shock motion at position (21, 3)

To study the correlation between vortex rings and the shock motion, we fix a position in the interaction region at (x, y) = (21, 3) on the path of the travelling of vortex rings (Figure 4-15 left). We record 20000 data from t = 1840T. During this time, there are thousands of rings coming from the upstream, the strength of which can be captured by the Omega values. The shock motion is characterized by the pressure fluctuations. Figure 4-15 right gives the signals of Omega and pressure fluctuations. As we can see, at most of time the peaks of the Omega correspond to the valleys of pressure and vice versa. The statistical correlation is found to be -0.7986, which indicates a strong negative correlation between the propagation of vortex rings and the shock motion.

4.3.2 Power Spectral Analysis

In order to further reveal the relation between the shock motion and separation location, the power spectra are presented in Figure 4-16. The pressure fluctuation has most of its energy at low frequencies around Strouhal number $St = fh/u_\infty = 0.018$ where *h* is the characteristic length, and these frequencies are consistent with the range of frequencies found in the separation point.

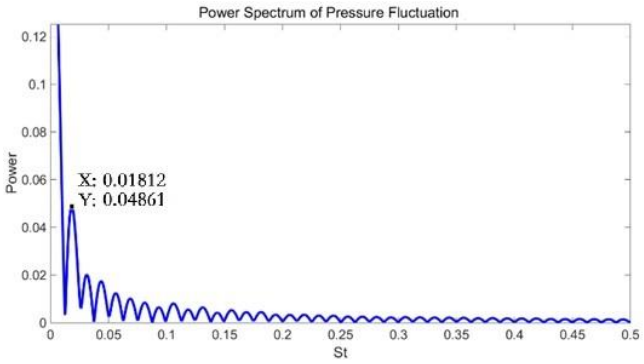

(a)

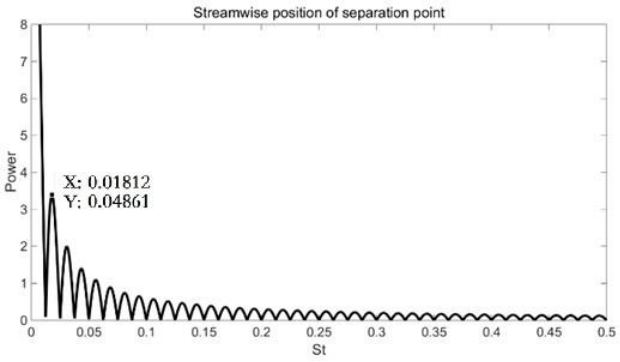

(b)

Figure 4-16 Power spectra of (a) pressure fluctuation and (b) separation location

4.3.3 Coherence between Vortex Rings and Shock Motion/Separation Bubble

During the shock ring interaction, the statistical relation between the vortex rings and the shock motion thus the separation bubble can also be investigated by means of

the coherence quantities. The coherence between two time signals $x(t)$ and $y(t)$ is defined as

$$r_{xy}^2(f) = \frac{\left|P_{xy}(f)\right|^2}{P_{xx}(f)P_{yy}(f)},$$

where $P_{xx}(f)$ denotes the power spectral density of signal $x(t)$, and $P_{xy}(f)$ denotes the cross power spectral density between signals $x(t)$ and $y(t)$. For all the frequency *f*, we have $0 \leq r_{xy}^2(f) \leq 1$. If $r_{xy} = 1$, then the signals $x(t)$ and $y(t)$ are linearly related at frequency *f*; if $r_{xy} = 0$, they are unrelated.

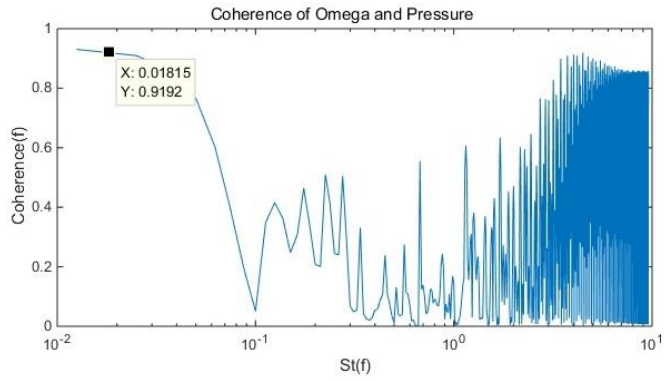

(a)

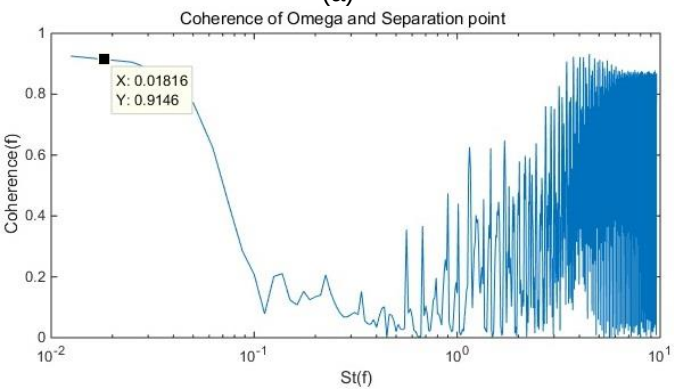

(b)

Figure 4-17 Coherence between (a) vortex rings and shock motion

(b) vortex rings and separation location

Using the 20000 data starting from t = 1840T, the coherences are calculated and the results are shown in Figure 4-17. Part (a) gives the coherence distribution between the vortex rings and shock motion at different Strouhal numbers, while part (b) gives the coherence between the rings and separation point. Very high values of coherence are observed in both figures at low frequencies, indicating that the rings and separation signals are almost linearly related. The shapes of the two coherence distributions are almost the same except that the coherences between rings and shock motion are higher at $0.1 \leq St \leq 0.5$, because the vortex rings have a direct interaction with the shock but indirectly influence the separation bubble.

Chapter 5

Conclusions and Discussion

Vortex is a very common phenomenon in nature, from tornado to turbulence. Detection and visualization of vortices is of critical importance in fluid dynamics since vortices carry most of the energy of vortical flows and thus contribute considerably to the flow evolution.

In this dissertation, several widely used techniques for vortex visualization in turbulent flows are reviewed and discussed. Three vortex identification methods, namely λ_2 method, Q method, and Omega method, are compared by visualization of several examples studied by direct numerical simulation (DNS) and large eddy simulation (LES) for flows with different speeds. The comparisons show the Omega method is much close to give vortex a mathematical definition and better visualization for vortical structures. The Omega method is quite universal and has no need to set up a threshold case by case. Additional advantages include easiness to perform, clear physical meaning, and high capability to capture both strong and weak vortices, which make Omega the most effective and efficient tool in vortex identification.

We apply the Omega method on the shock wave vortex ring interaction for the MVG controlled supersonic ramp flow. As the flow passes through the shock wave, its properties will change dramatically and discontinuously. The interaction between the oblique shock and vortex rings is investigated using the monotone integrated LES with fifth-order WENO scheme. By tracking a typical vortex ring when it passes through the shock, it is found that the spanwise vorticity takes a leading role in flow propagation, the topology of vortex rings is kept well but not rotate as fast as before, the separation shock gets distorted after hit by rings and sweeps back and forth, and a number of weak shocks exist around ring heads in the downstream.

Two thousands flow files are recorded to perform quantitative frequency analysis. A strong statistical correlation between the propagation of vortex rings and the shock motion is found to exist near the separation zone. There is a high coherence between the motion of rings and the pulsation of separation bubbles at low frequencies. It is possible that the shock ring interaction creates substantial low-frequency unsteadiness in the upstream region of the separation zone.

Since the boundary layer separation is induced by the shock wave, it is suggested that when the shock gets broken, the shock-induced flow separation will be reduced. The study of shock ring interaction reveals a great deal about instantaneous flow behavior, and thus will provide an insight on flow control.

References

[1] Adrian, R. J., “Hairpin vortex organization in wall turbulence”, Phys. Fluids, 19:1–16, 2007

[2] Robinson,S.K., “Coherent motions in the turbulent boundary layer”, Ann. Rev. Fluid Mech., 23: 601-639, 1991

[3] Bake, S., Meyer, D.G.W., and Rist, U., “Turbulent mechanism in Klebanoff transition: a quantitative comparison of experiment and direct numerical simulation”, J. Fluid Mech., 459: 217-243, 2002

[4] Perry, A.E., and Chong, M.S., “On the mechanism of wall turbulence”, J. Fluid Mech., 119: 173-217, 1982

[5] Adrian, R.J., Meinhart, C.D., and Tomkins, C.D., “Vortex organization in the outer region of the turbulent boundary layer”, J. Fluid Mech., 422: 1-54, 2000

[6] Alfonsi, G., and Primavera L., “Vortex Identification in the wall region of turbulent channel flow”, Comp. Sci. ICCS, pp 9-16, 2007

[7] Linnick, M., and Rist, U., “Vortex identification and extraction in a boundary layer flow”, Vision, Modeling, and Visualization, pp 9-16, 2005

[8] Tanaka, M., and Kida, S., “Characterization of vortex tubes and sheets”, Phys. Fluids, 5: 2079-2082, 1993

[9] Chong, M.S., Perry, A.E., and Cantwell, B.J., “A general classification of three dimensional flow fields”, Phys. of Fluid, 2: 765-777, 1990

[10] Jeong, J., and Hussain, F., “On the identification of a vortex”, J. Fluid Mech., 285: 69-94, 1995

[11] Kida, S., and Miura, H., “Identification and analysis of vortical structures”, Eur. J. Mech. B/Fluids, 17: 471-488, 1998

[12] Haller, G., “An objective definition of a vortex”, J. Fluid Mech., 525: 1-26, 2005

[13] Zhou, J., Adrian, R.J., Balachandar, S. and Kendall, T.M., “Mechanisms for generating coherent packets of hairpin vortices”, J. Fluid Mech., 387: 353-396, 1999

[14] Cucitore, R., Quadrio, M., and Baron, A., “On the effectiveness and limitations of local criteria for the identification of a vortex”, Eur. J. Mech. B/Fluids, 18: 261-282, 1999

[15] Kolar, V., “Vortex identification: new requirements and limitations”, International J. of Heat and Fluid Flow, 28: 638-652, 2007

[16] Chakraborty, P., Balachandar, S., and Adrian, R.J., “On the relationships between local vortex identification schemes”, J. Fluid Mech., 535: 189-214, 2005

[17] Yan, Y., Chen, C., Fu, H., and Liu, C., “DNS study on Λ-vortex and vortex ring formation in flow transition at Mach number 0.5”, J. Turbul., 15:1-21, 2014

[18] Lu, P., Yan, Y., Liu, C., “Numerical investigation on mechanism of multiple vortex rings formation in late boundary-layer transition”, Computers & Fluids, 71: 156-168, 2013

[19] Liu, C. and Chen, L., “Study of mechanism of ring-like vortex formation in late flow transition”, AIAA 2010-1456

[20] Rist. U, “Visualization and Tracking of vortices and shear layers in the late stages of boundary layer laminar-turbulent transition”, AIAA 2012-84

[21] Yan, Y., and Liu, C., “Study on the initial evolution of ring-like vortices generated by MVG”, CEAS Aeronaut J., 4: 433-442, 2013

[22] Li, Q., Yan, Y., and Liu, C., “Numerical and experimental studies on the separation topology of the MVG controlled flow”, AIAA 2011-72

[23] Yan Y., Kaur A., Tang J. and Liu, C., “DNS Study on Mechanism of Formation of Lambda Rotational Core in Late Boundary Layer Transition”, AIAA paper, 2014-1134

[24] Yan, Y., Wang, X., Liu, C., “LES and analyses on the vortex structure behind supersonic MVG with turbulent inflow”, Appl. Math. Model., 38: 196-211, 2014

[25] Yan, Y., Chen, C., Lu, P, and Liu, C., “Study on shock wave-vortex ring interaction by the micro vortex generator controlled ramp flow with turbulent inflow”, Aerospace Science and Technology, 30: 226–231, 2013

[26] Yan, Y., Li, Q., Liu, C., Pierce, A., Lu, F., and Lu, P., “Numerical discovery and experimental confirmation of vortex ring generation by microramp vortex generator”, Applied Mathematical Modelling, 36: 5700–5708, 2012

[27] C. Liu, Y. Wang, Y. Yang, and Z. Duan, “New Omega Vortex Identification Method”, Sci. CHINA Physics, Mech. Astron., Vol. 59, No. 8, pp. 684-711, 2016

[28] J. C. R. Hunt, A. A. Wray, and P. Moin, “Eddies, Streams, and Convergence Zones in Turbulent Flows” in Center for Turbulence Research, Proceedings of the Summer Program, pp. 193–208, 1988

[29] B. Pierce, P. Moin, and T. Sayadi, “Application of Vortex Identification Schemes to Direct Numerical Simulation Data of a Transitional Boundary Layer”, Physics of Fluids 25, 015102, 2013

[30] C. Liu, Y. Yan, and P. Lu, “Physics of turbulence generation and sustenance in a boundary layer”, Computers & Fluids, 102: 353-384, 2014

[31] Y. Wang, H. Al-dujaly, Y. Yan, N. Zhao, and C. Liu, “Physics of multiple level hairpin vortex structures in turbulence”, Science China Physics, Mechanics & Astronomy, 59(2): 1-11, 2016

[32] P. Lu, and C. Liu, “DNS Study on Mechanism of Small Length Scale Generation in Late Boundary Layer Transition”, Physica D 241: 11-24, 2012

[33] C. Liu, and L. Chen, “Parallel DNS for Vortex Structure of Late Stages of Flow Transition, J. of Computers and Fluids”, Vol.45, pp. 129-137, 2011

[34] F. Lu, Q. Li, and C. Liu, “Micro Vortex Generators in High-Speed Flow”, Journal of Progress in Aerospace Science, Vol. 53, pp. 30–45, 2012

[35] C. Liu, and Z. Liu, “Multigrid Mapping and Box Relaxation for Simulation of the Whole Process of Flow Transition in 3-D Boundary Layers”, J. of Computational Physics, Vol. 119, pp. 325-341, 1995

[36] Y. Dong, Y. Yan, and C. Liu, “New Visualization Method for Vortex Structure in Turbulence by Lambda2 and Vortex Filaments”, Journal of Applied Mathematical Modelling, 40(1): 500-509, 2016

[37] Q. Li, and C. Liu, “Implicit LES for Supersonic Microramp Vortex Generator: New Discoveries and New Mechanisms”, Modelling and Simulation in Engineering, Volume 2011, Article ID 934982, 2011

[38] Q. Li, and C. Liu, “Numerical Investigations on the Effects of the Declining Angle of the Trailing-Edge of MVG”, AIAA Journal of Aircraft, Vol. 47, No. 6, pp. 2086-2095, 2011

[39] Q. Li, Y. Yan, C. Liu and F. Lu, “Separation Topology of Microramp Vortex Generator Controlled Flow at Mach Number 2.5”, Journal of Aircraft C033280, Vol. 52, Issue 6, pp. 2095-2100, 2015

[40] Z. Sun, F. Scarano, B. W. van Oudheusden, Ferry F. J. Schrijer, Y. Yan, and C. Liu, “Numerical and Experimental Investigations of the Supersonic Microramp Wake”, AIAA Journal, Vol. 52, No. 7, 2014

[41] Yan, Y., Tang, J., Liu, C., and Yang, F., "DNS study on the formation of Lambda rotational core and the role of TS wave in boundary layer transition", Journal of Turbulence, Vol. 17, No. 6, pp. 572-601, 2016

[42] Liu, C., Wang, Y., and Tang, J., “New Vortex Identification Method and Vortex Ring Development Analysis in Boundary Layer Transition”, 54th AIAA Aerospace Sciences Meeting, pp. 2068, 2016

[43] Tang, J., Yang, Y., Yan, Y., and Liu, C., “DNS study on role of linearly unstable modes in flow transition”, AIAA paper, 2015-0585

[44] Wang, Y., Al-Dujaly, H., Tang, J., and Liu, C., “DNS study on hairpin vortex structure in turbulence”, In 53rd AIAA Aerospace Sciences Meeting, 2015

[45] Yan, Y., Tang, J., Kaur, A., and Liu, C., “DNS study for mechanism of formation of lambda rotational core and ring-like vortex in late boundary layer transition”, In 52nd AIAA Aerospace Sciences Meeting, 2014

[46] Yang, Y., Tang, J., Yan, Y., and Liu, C., “DNS Study on Mechanism of Flow Chaos in Late Boundary Layer Transition”, Chaotic Modeling and Simulation Journal, 2: 157–168, 2015

[47] J. D. Anderson, “Fundamentals of Aerodynamics”, 5th Edition, McGraw-Hill Education, 2012

[48] S. M. Hirt, D. B. Reich, and M. B. O'Connor, "Micro-ramp Flow Control for Oblique Shock Interactions: Comparisons of Computational and Experimental Data", 5th Flow Control Conference, AIAA 2012-4973

[49] F. Lu, Q. Li, and C. Liu, “Micro vortex generators in high-speed flow”, Progress in Aerospace Sciences, Vol. 53, pp. 30-45, 2012

[50] H. Babinsky, Y. Li, and C. W. Pitt Ford, "Microramp Control of Supersonic Oblique Shock-Wave/Boundary-Layer Interactions", AIAA Journal, Vol. 47, No. 3, pp. 668-675, 2009

[51] J. C. Lin, “Review of Research on Low-profile Vortex Generators to Control Boundary-layer Separation”, Progress in Aerospace Sciences, 38: 389-420, 2002

[52] N. T. Clemens, and V. Narayanaswamy, “Low Frequency Unsteadiness of Shock Wave /Turbulent Boundary Layer Interactions”, Annu. Rev. Fluid Mech., 46: 496-492, 2014

[53] Y. Yang, Y. Yan, and C. Liu, “LES Study on Mechanism of Reduction of Shock Induced Flow Separation by MVG”, AIAA paper, 2015-1240

[54] S. Zhang, Y. Zhang, and C. Shu, “Multistage Interaction of a Shock Wave and a Strong Vortex”, Physics of Fluids, 17: 116101, 2005

[55] S. M. Chang, and K. S. Chang, “Visualization of Shock-vortex Interaction Radiating Acoustic Waves”, Journal of Visualization, Vol. 3, Issue 3, pp. 221-228, 2000

[56] O. Inoue, and Y. Hattori, “Sound Generation by Shock-vortex Interactions”, J. Fluid Mech., Vol. 380, pp. 81-116, 1999

[57] S. Priebe, and M. P. Martin, “Low Frequency Unsteadiness in Shock Wave-Turbulent Boundary Layer Interaction”, J. Fluid Mech., Vol. 699, pp. 1-49, 2012

[58] M. Grilli, P. J. Schmid, S. Hickel, and N. A. Adams, “Analysis of Unsteady Behavior in Shockwave Turbulent Boundary Layer Interaction”, J. Fluid Mech., Vol. 700, pp. 16-28, 2012

[59] R. H. M. Giepman, F. F. J. Schrijer, and B. W. van Oudheusden, “Flow Control of an Obilique Shock Wave Reflection with Micro-ramp Vortex Generators: Effects of Location and Size”, 5th European Conf. for Aeronautics and Space Sciences, 2013

[60] S. Lee, M. K. Goettke, E. Loth, J. Tinapple, and J. Benek, “Microramps Upstream of an Oblique-Shock/Boundary-Layer Interaction”, AIAA Journal, 48(1): 104-118, 2010

[61] S. Ghosh, J. Choi, and J. R. Edwards, “Numerical Simulations of Effects of Micro Vortex Generators Using Immersed-Boundary Methods”, AIAA Journal, 48(1): 92-103, 2010

[62] C. Liu, Y. Yan, and P. Lu, “Physics of Turbulence Generation and Sustenance in a Boundary Layer”, Computers & Fluids, 102: 353–3841, 2014

[63] S. E. Guarini, R. D. Moser, K. Shariff, and A. Wray, “Direct Numerical Simulation of a Supersonic Turbulent Boundary Layer at Mach 2.5”, J. Fluid Mech., Vol. 414, pp. 1-33, 2000

[64] Y. Yan, and C. Liu, “Origin of Ring-like Vortices in the MVG Controlled Turbulent Boundary Layer”, AIAA paper, 2013-0400

[65] M. R. Saad, H. Zare-Behtash, A. Che-Idris, and K. Kontis, “Micro-Ramps for Hypersonic Flow Control”, Micromachines, 3: 364-378, 2012

[66] Z. Sun, “Micro Vortex Generators for Boundary Layer Control: Principles and Applications”, International Journal of Flow Control, Vol. 7, Issue 1-2, pp. 67-86, 2015

[67] Z. Sun, F. F. J. Schrijer, F. Scarano, and B. W. van Oudheusden, “The Three-dimensional Flow Organization Past a Micro-ramp in a Supersonic Boundary Layer”, Physics of Fluids, 24: 055105, 2012

[68] F. Lu, Q. Li, Y. Shih, A. J. Pierce, and C. Liu, “Review of Micro Vortex Generators in High-speed Flow”, AIAA paper, 2011-31

[69] Y. Yang, Y. Yan, and C. Liu, “ILES for Mechanism of Ramp-type MVG Reducing Shock Induced Flow Separation”, SCIENCE CHINA Physics, Mechanics & Astronomy, 59 (12), 124711, 2016

[70] Yang, G., Yao, Y., Fang, J., Gan, T., Lu, L., and Yang, Y, Large-Eddy Simulation of Shock-Induced Flow Separation Control Using SparkJet Concept, In 54th AIAA Aerospace Sciences Meeting, 2015

[71] Dong, Y., Dong, X., Yang, Y., and Liu, C., “Numerical Investigation on the Oblique Shock and High-speed Vortex Rings Interaction”, 55th AIAA Aerospace Sciences Meeting, AIAA SciTech Forum, AIAA 2017-0137

[72] Yang, Y., Yan, Y., and Liu, C., “Optimization of MVG Position for Control of Shock Boundary Layer Interaction”, In 53rd AIAA Aerospace Sciences Meeting (pp. 1–12), Orlando, Florida: American Institute of Aeronautics and Astronautics, 2015

[73] Wallace, J.M., “Highlights from 50 years of turbulent boundary layer research”, Journal of Turbulence, 13, N53, 2012

[74] Yang, Y., Tang, J., and Liu, C., “LES Analysis on Shock-Vortex Ring Interaction”, In 54th AIAA Aerospace Sciences Meeting (pp. 1–13), San Diego, California: American Institute of Aeronautics and Astronautics, 2016

[75] Dong, Y., Yang, Y., and Liu, C., “DNS Study on Three Vortex Visualization Methods”, 55th AIAA Aerospace Sciences Meeting, AIAA SciTech Forum, AIAA 2017-0490

[76] Babinsky, H., and Harvey, J.K., “Shock Wave-Boundary-Layer Interactions”, Cambridge University Press, 2011

Biographical Information

Yinlin Dong grew up in Tianjin, China and attended Nankai University, where he earned his B.S. degree in computational mathematics. He pursued an M.A. degree in mathematics at the University of Alabama. His family then lived in Orlando, Florida, for two years. He moved to Texas in 2013 and complete his Ph.D. in mathematics at the University of Texas at Arlington in August 2017. He has been teaching a wide range of undergraduate math courses for seven years. His research interests include numerical methods, computational fluid dynamics, and statistical analysis.